RESEARCH ARTICLE

WILEY

Extension of the two-component pressure approach for modeling mixed free-surface-pressurized flows with the two-dimensional shallow water equations

Luis Cea[1,2] | Alejandro López-Núñez[2]

[1]E.T.S. Ingenieros de Caminos Canales y Puertos, Universidade da Coruña, A Coruña, Spain

[2]Environmental and Water Engineering Group (GEAMA), Universidade da Coruña, A Coruña, Spain

Correspondence
Luis Cea, E.T.S. Ingenieros de Caminos Canales y Puertos, Universidade da Coruña, A Coruña 15071, Spain.
Email: luis.cea@udc.es

Abstract

Numerical models based on the two-dimensional shallow water equations (2D-SWE) are routinely used in flood risk management and inundation studies. However, most of these models do not adequately account for vertically confined flow conditions that can appear during inundations, due to the presence of hydraulic structures such as bridges, culverts, or underground river reaches. In this article we propose a new mathematical modification of the standard 2D-SWE, inspired by the two-component pressure approach for 1D flows, to address the issue of transient vertically confined flows including transitions between free surface and pressurized conditions. A finite volume discretization to solve the proposed system of equations is proposed and analyzed. Various test cases are used to show the numerical stability and accuracy of the discretization, and to validate the proposed formulation. Results show that the proposed method is numerically stable, accurate, mass conservative, and preserves the C-property. It can also handle subcritical, supercritical, and transcritical flows under free surface or vertically confined conditions.

KEYWORDS

2D shallow water equations, finite volume method, free surface flow, pressurized flow, two-component pressure approach

1 | INTRODUCTION

Improvements achieved over recent years on the accuracy, stability, and computational efficiency of the numerical schemes used to solve the two-dimensional depth-averaged shallow water equations (2D-SWE) have led to their routine application in flood risk management and inundation forecasting studies.[1-6] One of the main approximations carried out in the derivation of the 2D-SWE is that the pressure distribution is hydrostatic.[7-9] However, during a flood event the occurrence of pressurized flows at certain locations is quite common, due to the presence of hydraulic structures such as bridges, culverts, or underground river reaches in urban areas. At these locations the standard 2D-SWE are no longer

valid unless they are modified to take into account the vertical confinement of the flow. In the specific case of submerged bridges, the effect of the deck is often modeled with empirical one-dimensional (1D) discharge equations (or rating curves) which relate the head loss to the water discharge through the bridge.[10-12] With this approximation the deck is modeled as a thin line in the numerical mesh, and its width in the flow direction is neglected. One limitation of this approach is that the discharge equations available are only strictly valid when the flow is mostly 1D and perpendicular to the bridge deck. In the case of culverts across bridge embankments and in underground rivers in urban areas, the discharge is usually approximated with algebraic equations based on Manning's formula or at best using the 1D-SWE. In the latter case the original 1D-SWE, valid only for free surface flows, must be modified in order to account for pressurized conditions. Also, it should be noted that when using empirical or theoretical 1D discharge equations to model bridges or culverts, steady flow conditions are assumed.

Several approaches have been proposed to modify the original 1D-SWE in order to account for pressurized conditions. Here we include some highlights of various different approaches, but for a thorough description, the reader is referred to the study of Reference 13.

The most classic and widespread method is the Preissmann slot method (PSM), first proposed by Cunge and Wegner.[14] The PSM is a one-equation model that consists of adding a hypothetical, indefinitely extended slot to the crown of the conduit.[13,15] It is a relatively simple method and produces consistent results in the transition from free surface to pressurized conditions.[15,16] The width of the slot is the main numerical parameter of the method, and its value can be theoretically fixed so that the celerity of the pressure waves in a close conduit is correctly reproduced. However, this usually implies very small values of the slot width, and it can lead to spurious numerical oscillations.[17] On the other hand, if the width of the slot is large the pressurized wave celerity will generally be underpredicted and there will be a loss of water mass through the slot. In practice, the Preissmann slot width is set as a percentage of the pipe or channel width (usually in the order of 0.01), and it is not necessarily related to any physical property of the conduit. The choice of its value is in general justified as a good compromise between accuracy, numerical stability, and computational efficiency.[18] Another drawback of this method is that it introduces an artificial free surface flow regeneration, even when the ventilation is insufficient.[13]

Other one-equation models exist as alternatives to the PSM, such as the two-component pressure approach (TPA) proposed by Vasconcelos et al..[19] This method overcomes the problem of the artificial free surface flow regeneration by considering the total pressure as the sum of two components, a hydrostatic pressure and a dynamic pressure. The method assumes certain elasticity of the conduit and neglects the compressibility of water. Using the water hammer equations for 1D pipes, the conduit elasticity is related to the wave celerity under pressurized conditions, which is the numerical parameter of the method. The TPA is capable of handling negative pressures, although it can lead to spurious numerical oscillations in cases with a high wave celerity. For that reason, even though the wave celerity in pressurized closed conduits may attain values of 1000 m/s under real conditions,[20] the used values lay between 25 and 100 m/s in practical test cases (well below physically realistic values), which is justified in terms of computational efficiency (CPU time) and numerical accuracy. These relatively low values of the wave celerity reduce spurious oscillations and avoid numerical instabilities. Larger values of the wave speed would significantly increase the CPU time without improving numerical accuracy in the prediction of free surface-pressurized flow transitions.[16,18,20]

Another approach to the problem is the use of a semiimplicit discrete equation for pressure as in Reference 21. This approach is interesting since it does not need to resort to any artificial parameter to compute the pressure under confined conditions.

Also worth mentioning are the two-equation methods, the most common of which are the interface tracking models, the rigid column based models, and the finite-volume two-equation methods. The interface tracking models,[22-24] involve treating each of the sides of the wavefronts separately, usually by applying the method of characteristics. However, these methods tend to require small time steps in the pressurized region to fulfill the CFL condition, thus increasing computational time. Also, the method of characteristics can cause instabilities when there are large discontinuities at the interface or when the differences between the velocity or piezometric head in the two waves are significant.

Right column based models,[25-28] consider an air phase motion induced by the wavefront motion and use the Helmholtz instability condition to discriminate the state of the air (pressurized or not). However, an important limitation of this model is that it is applied only for a single air pocket and it is not easy to incorporate the presence of multiple air pockets into the equations.

Finally, finite-volume two-equation methods are in most cases conservative. Among these, the most common include the model proposed by Bourdarias and Gerbi,[29] which considers the momentum flux, pressure, and friction as continuous at the interface between pressurized flow and free surface flow; and the Illinois transient model by Leon and Oberg,[30] a multipurpose finite-volume, shock-capturing model capable of analyzing a wide range of mixed flows. However,

finite-volume two-equations models are mathematically complex and present considerable difficulties in their implementation, requiring robust and efficient solvers. Because of this, it is usually necessary to include certain assumptions that lower the complexity of the model at the cost of a loss accuracy in the solution. This balance can be difficult to address.

However, 1D approximations are not suitable for cases in which 2D flow patterns develop within the flow. Some examples here are culverts with a large width-to-length ratio, bridges in which the flow is nonuniform over the bridge length, or sharp junctions in underground river reaches, among others. In addition, merging 1D and 2D approaches in the same model always has the inconvenience of coupling the interactions between 1D and 2D mesh elements, especially when the 1D cross-section is large compared with the mesh size used in the 2D model. In the previous cases it is useful to model the pressurized flow with a more realistic 2D approximation. However, to our knowledge the only attempt to adapt the 2D-SWE to pressurized conditions is the extension of the Preissmann slot method to 2D transient mixed flows presented in Reference 18. In the current article we propose a new method to account for vertically confined flows in the 2D-SWE. The method is similar in concept to the TPA used in Reference 19 for the 1D-SWE in the sense that it includes in the momentum conservation equations an additional pressure term that is computed as a function of the water depth and a stiffness constant. The modified shallow water equations and the discretization scheme used to solve them are presented in Sections 2 and 3, respectively. The performance of the proposed model is tested against analytical and reference solutions in Section 4. Finally, the main conclusions of the study are summarized in Section 5.

2 | MODEL EQUATIONS

2.1 | Modified 2D shallow water equations

The 2D-SWE are a set of three hyperbolic differential equations which express the conservation of water mass and linear momentum in the x and y directions.[31] The forces that are usually considered in the momentum conservation equations are the bed friction and the net hydrostatic pressure force (which is generated by gravity). The hydrostatic pressure assumption implies that the net pressure force originated by the hydrostatic pressure gradient and exerted over a water column of 1 m width depends only on the free surface gradient, on the water depth, and on the gravity acceleration. This is valid as long as the vertical accelerations are negligible and the water surface is free to move up and down without any physical restriction. A consequence of this assumption is that free surface perturbations in still water propagate with a wave celerity equal to $c_w = \sqrt{gh}$, where h is the water depth and g is the gravity acceleration.[8,9,31]

In the presence of a solid roof, the water depth is constrained by the roof height, which exerts a pressure force and a friction force on the water surface (which is no longer free). In such a case, the water surface cannot move freely, and the 2D-SWE cannot be directly applied. In order to deal with these effects we propose the introduction of an additional pressure term, and a modification of the friction term in the standard depth averaged momentum equations, which would then read:

$$\frac{\partial h}{\partial t} + \frac{\partial q_x}{\partial x} + \frac{\partial q_y}{\partial y} = 0, \tag{1}$$

$$\frac{\partial q_x}{\partial t} + \frac{\partial}{\partial x}\left(\frac{q_x^2}{h} + \frac{gh^2}{2}\right) + \frac{\partial}{\partial y}\left(\frac{q_x q_y}{h}\right) = -gh\frac{\partial z_b}{\partial x} - ghI_x - \frac{h}{\rho}\frac{\partial P_s}{\partial x}, \tag{2}$$

$$\frac{\partial q_y}{\partial t} + \frac{\partial}{\partial x}\left(\frac{q_x q_y}{h}\right) + \frac{\partial}{\partial y}\left(\frac{q_y^2}{h} + \frac{gh^2}{2}\right) = -gh\frac{\partial z_b}{\partial y} - ghI_y - \frac{h}{\rho}\frac{\partial P_s}{\partial y}, \tag{3}$$

where z_b is the bed elevation, h is the water depth, (q_x, q_y) are the two components of the unit discharge, (I_x, I_y) are the two components of the friction slope (including bed friction and roof friction), g is the gravity acceleration, ρ is the water density, and P_s is the pressure applied on the water surface by the solid roof. The surface pressure (last term on the right-hand side of the momentum equations) is usually included in the shallow water equations in order to account for spatial variations on atmospheric pressure,[32-36] but it is used here to account for the pressure applied by the roof on the water surface.

In this study we will use Manning's equation to compute the bed and roof friction slope. In order to account for the bed and roof friction at the same time, the friction slope is computed as:

$$I_x = \frac{n_c^2 |\mathbf{U}| U_x}{R_h^{(4/3)}} \quad I_y = \frac{n_c^2 |\mathbf{U}| U_y}{R_h^{(4/3)}}, \tag{4}$$

where n_c is a bed-roof composite roughness, R_h is a hydraulic radius, (U_x, U_y) are the two components of the depth averaged velocity, and $|\mathbf{U}|$ is its modulus. In free surface regions the composite roughness and the hydraulic radius are equal to the bed roughness and the water depth, respectively, and Equation (4) reduces to the bed friction slope used in the standard 2D-SWE. However, in pressurized regions both values are modified in order to account for the effect of the solid roof. Several formulas have been proposed to compute a composite roughness in compound channels.[37] Here, we have used the formulation proposed in Reference 38, in which the composite roughness is computed as a wet-perimeter weighted average of the different Manning coefficients. This formulation assumes that the total shear velocity is the weighted sum of the subareas' shear velocities. Applied to a small region of fluid with horizontal area A and water depth h, the composite roughness and hydraulic radius are then computed as:

$$n_c = \begin{cases} n_s & \text{if } h \le z_r - z_b \\ \frac{n_s A + n_r A}{2A} = \frac{n_s + n_r}{2} & \text{if } h > z_r - z_b \end{cases} \quad R_h = \begin{cases} h & \text{if } h \le z_r - z_b \\ \frac{hA}{2A} = \frac{h}{2} & \text{if } h > z_r - z_b \end{cases}, \quad (5)$$

where n_s and n_r are, respectively, the Manning coefficients of the bed and roof, and z_r is the roof height.

In addition to the bed and roof friction, the lateral vertical walls also produce a friction force in the fluid. In order to account for the friction generated by the solid boundary walls, following again the formulation proposed in Reference 38, the composite roughness and hydraulic radius at the boundary mesh elements are computed as:

$$n_{c,w} = \begin{cases} \frac{n_s A + n_w L_w h}{A + L_w h} & \text{if } h \le z_r - z_b \\ \frac{n_s A + n_r A + n_w L_w h}{2A + L_w h} & \text{if } h > z_r - z_b \end{cases} \quad R_{h,w} = \begin{cases} \frac{hA}{A + L_w h} & \text{if } h \le z_r - z_b \\ \frac{hA}{2A + L_w h} & \text{if } h > z_r - z_b \end{cases}, \quad (6)$$

where A is the horizontal area of the boundary mesh element, L_w is the length of the element edge in contact with the wall, and n_w is the Manning coefficient of the lateral solid wall. Equation (4) is replaced by Equation (6) only in the mesh elements in contact with a boundary solid wall.

2.2 | Estimation of the pressure stress on the solid roof

To complete the system of Equations (1–3), a formulation to compute the pressure stress on the roof must be provided. The surface pressure P_s is zero in regions where the water surface elevation ($z_s = z_b + h$) is lower than the roof elevation (z_r), and positive in regions where the water depth is constrained by the roof. In the latter case, the magnitude of P_s must be such that the water depth predicted by Equation (1) remains equal to the roof height (h_r), defined as the difference between the roof elevation, and the bed elevation ($h_r = z_r - z_b$). One possible way to solve the system given by Equations (1–3) in vertically confined regions is to use an implicit algorithm for pressure-linked equations, in a way similar to how SIMPLE, SIMPLEC, or PISO algorithms are used to solve the incompressible Navier–Stokes equations.[39] In that case, the water depth would be known and equal to the roof height, and the unknowns of the system would be the unit discharges and the roof pressure. Such an approach would be complicated to implement in mixed flow conditions, and would be difficult to incorporate into existing 2D finite volume shallow water codes, which in most cases are explicit in time. Thus, we propose to relax this condition by allowing for small differences between the computed water depth and the roof height (Figure 1), and to compute the surface pressure as:

$$P_s = \rho K_r (h - h_r) = \rho K_r H_s \quad H_s = h - h_r, \quad (7)$$

where H_s is the difference between the water depth computed with the 2D-SWE and its exact value under submerged roofs (h_r), and K_r is a stiffness constant expressed in m/s^2. This approach is similar to the introduction of a certain degree of elasticity on the solid roof, in the same way as the cross-section elasticity considered in the 1D TPA of Reference 19. The surface pressure is directly proportional to the vertical deformation of the roof. The value of the stiffness constant should be fixed according to accuracy and numerical stability criteria and thus, it does not represent the real stiffness of the roof. A low value of K_r will allow for large differences between h and h_r (which are obviously not real, but simply needed for numerical discretization), while a high stiffness constant will limit the differences between h and h_r, producing more

FIGURE 1 Schematic representation of mixed flow conditions including a region under pressure and a region under free surface [Colour figure can be viewed at wileyonlinelibrary.com]
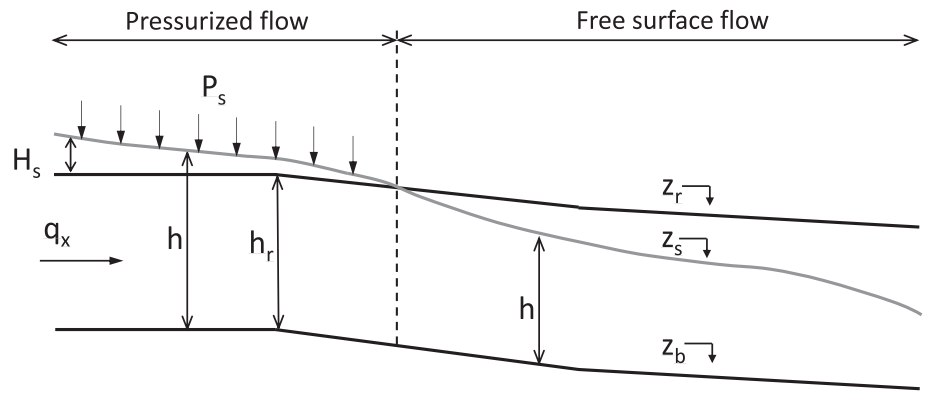
accurate results at the cost of reducing the integration time step needed to achieve numerical stability. The effect of K_r on the numerical stability and accuracy of the scheme will be shown and discussed in the following sections.

Equation (7) is valid in regions where the flow is under pressure ($h \geq h_r$), but it must be modified to properly account for free surface conditions ($h < h_r$). One possibility is to make $K_r = 0$ in free surface regions, but this would imply that K_r is variable in space and time, which complicates the numerical discretization of the surface pressure term. An alternative strategy, and the one adopted in the model proposed here, is to redefine the roof height (h_r) as the minimum between its real height and the water depth:

$$h_r = \min(h, z_r - z_b). \tag{8}$$

With the previous definition of h_r, the surface pressure computed from Equation (7) equals zero in free surface regions, since in those areas $h < z_r - z_b$ and thus, $h_r = h$ and $P_s = 0$ according to Equation (7). Using Equation (8) to define h_r at the same time in both free surface and pressurized regions is useful for two reasons: first, because the value of K_r can be taken as constant in space and time and thus we can remove it from the spatial derivative in the momentum conservation equations; and second, because it allows us to split the surface pressure term given by Equation (7) into two addends, one that depends only on geometrical parameters when the flow is pressurized ($-\rho K_r h_r$), and another which depends on the flow variables ($\rho K_r h$). As we will describe in detail in the following section, the first addend will be treated as a source term, while the second one will be discretized together with the convective flux.

Assuming a spatially constant value of K_r in Equation (7), the surface pressure term in the momentum equations is expressed as:

$$-\frac{h}{\rho}\frac{\partial P_s}{\partial x} = -K_r h \frac{\partial H_s}{\partial x} \qquad -\frac{h}{\rho}\frac{\partial P_s}{\partial y} = -K_r h \frac{\partial H_s}{\partial y}. \tag{9}$$

Note that the value of H_s is easily computed at each time step from the difference between the water depth predicted by Equation (1) and the roof height defined by Equation (8). Also note the similarity between this term and the bed slope source term in Equations (2–3). We will take advantage of this similarity in order to propose a numerical discretization of the equations in the next section.

2.3 | Complete system of equations

Taking into account the previous definitions for the pressure stress (Equation 9), which assume a spatially constant K_r, Equations (1–3) become:

$$\frac{\partial h}{\partial t} + \frac{\partial q_x}{\partial x} + \frac{\partial q_y}{\partial y} = 0, \tag{10}$$

$$\frac{\partial q_x}{\partial t} + \frac{\partial}{\partial x}\left(\frac{q_x^2}{h} + \frac{gh^2}{2}\right) + \frac{\partial}{\partial y}\left(\frac{q_x q_y}{h}\right) = -gh\frac{\partial z_b}{\partial x} - ghI_x - K_r h \frac{\partial H_s}{\partial x}, \tag{11}$$

$$\frac{\partial q_y}{\partial t} + \frac{\partial}{\partial x}\left(\frac{q_x q_y}{h}\right) + \frac{\partial}{\partial y}\left(\frac{q_y^2}{h} + \frac{gh^2}{2}\right) = -gh\frac{\partial z_b}{\partial y} - ghI_y - K_r h\frac{\partial H_s}{\partial y}. \tag{12}$$

Considering that $H_s = h - h_r$, Equations (10–12) can be rewritten as:

$$\frac{\partial h}{\partial t} + \frac{\partial q_x}{\partial x} + \frac{\partial q_y}{\partial y} = 0, \tag{13}$$

$$\frac{\partial q_x}{\partial t} + \frac{\partial}{\partial x}\left(\frac{q_x^2}{h} + \frac{(g+K_r)h^2}{2}\right) + \frac{\partial}{\partial y}\left(\frac{q_x q_y}{h}\right) = -gh\frac{\partial z_b}{\partial x} - ghI_x + K_r h\frac{\partial h_r}{\partial x}, \tag{14}$$

$$\frac{\partial q_y}{\partial t} + \frac{\partial}{\partial x}\left(\frac{q_x q_y}{h}\right) + \frac{\partial}{\partial y}\left(\frac{q_y^2}{h} + \frac{(g+K_r)h^2}{2}\right) = -gh\frac{\partial z_b}{\partial y} - ghI_y + K_r h\frac{\partial h_r}{\partial y}, \tag{15}$$

with h_r given by Equation (8) and with a value of K_r defined by the user.

2.4 | Wave celerity

Another important issue related to the new surface pressure term is that it affects the celerity at which pressure perturbations propagate within the flow. This is correct from a physical point of view, since the wave celerity in pressurized flows is much higher than in free surface flows. In the standard shallow water equations the free surface wave celerity is given by $c_w = \sqrt{gh}$. When the surface pressure term given by Equation (9) is included in the momentum equations, the wave celerity remains equal to $c_w = \sqrt{gh}$ when $h < z_r - z_b$ (free surface), but it increases to $c_w = \sqrt{(g+K_r)h}$ when $h \geq z_r - z_b$ (pressurized conditions). A simple way to derive the wave celerity under pressurized conditions is to make an analogy with the water hammer equations.[40] Assume an elastic pipe with rectangular cross-section of width B, height h, and area $A = Bh$, which is only deformed in the vertical direction, that is, $\Delta A = B\Delta h$. In such a case, assuming an incompressible fluid, the water hammer wave celerity is given by:

$$c_w = \sqrt{\frac{\Delta P}{\rho}\frac{h}{\Delta h}}, \tag{16}$$

where Δh is the increase in water depth induced by a roof pressure increase of ΔP. In our shallow water model, the increase in pressure over the water column is due to the gravity force and to the roof pressure, and is given by:

$$\frac{\Delta P}{\rho} = g\Delta h + K_r \Delta h. \tag{17}$$

Thus, the water hammer wave celerity simplifies to:

$$c_w = \sqrt{(g+K_r)h}. \tag{18}$$

It should be noted that the flux terms on the left-hand side of the momentum conservation equations reflect the change in wave celerity when including the surface pressure.

Using Equation (18), K_r could be fixed by the user in order to reproduce the physical wave celerity in close conduits. However, that would imply very high values of K_r and thus a high increase in CPU time and the possible appearance of numerical instabilities, without improving the numerical accuracy of the solution in most practical applications, since the integration time step depends on the wave celerity, as will be shown in the following section. This has also been noted by Sanders and Bradford[20] in the TPA method, using values of the wave celerity of an order of magnitude below physically realistic values, in order to obtain a compromise between computational efficiency and numerical accuracy. It is also the reason why the slot width in the Preissmann slot model is usually fixed to 0.01 times the channel width, in order to limit the wave celerity and numerical instabilities.[13,18]

3 | NUMERICAL SOLVER

In this section we will focus on the discretization of the new terms linked to the surface pressure and how these can be incorporated into a standard finite volume solver for the 2D-SWE. For this purpose we will use the unstructured finite volume solver for the 2D-SWE implemented in the software Iber.[10] In this solver, the momentum flux is discretized with an explicit Godunov-type scheme based on the approximate Riemann solver of Roe.[41,42] Since the scheme is explicit, the computational time step used to advance the solution in time is limited by the Courant–Friedrichs–Lewy (CFL) stability constraint,[43] which establishes a relation between the maximum permissible computational time step, the grid size, the flow velocity, and the wave celerity. The bed elevation source term is discretized with an upwind scheme that ensures an exact balance of the equations under hydrostatic conditions.[44] A semiimplicit scheme is used to discretize the bed friction source term in order to enhance the numerical stability of the solver. Both, the upwind discretization of the bed slope and the semiimplicit discretization of the friction term are common practice in finite volume solvers for the shallow water equations.[45-50] The proposed numerical scheme is first order in time.

3.1 | Numerical discretization

Compared with the standard SWE, Equations (13–15) introduce the stiffness constant K_r in the definition of the momentum flux terms on the left-hand side of the momentum conservation equations, and at the same time they include a new source term that involves the stiffness constant K_r and the roof height h_r as defined in Equation (8). The system of Equations (13–15) can be written in vectorial form as:

$$\frac{\partial w}{\partial t} + \frac{\partial F_x}{\partial x} + \frac{\partial F_y}{\partial y} = \mathbf{S} + \mathbf{T} + \mathbf{P},$$

(19)

$$\mathbf{w} = \begin{pmatrix} h \\ q_x \\ q_y \end{pmatrix} \quad \mathbf{F_x} = \begin{pmatrix} q_x \\ \frac{q_x^2}{h} + \frac{(g+K_r)h^2}{2} \\ \frac{q_x q_y}{h} \end{pmatrix} \quad \mathbf{F_y} = \begin{pmatrix} q_y \\ \frac{q_x q_y}{h} \\ \frac{q_y^2}{h} + \frac{(g+K_r)h^2}{2} \end{pmatrix},$$

$$\mathbf{S} = \begin{pmatrix} 0 \\ -gh\frac{\partial z_b}{\partial x} \\ -gh\frac{\partial z_b}{\partial y} \end{pmatrix} \quad \mathbf{T} = \begin{pmatrix} 0 \\ -ghI_x \\ -ghI_y \end{pmatrix} \quad \mathbf{P} = \begin{pmatrix} 0 \\ hK_r\frac{\partial h_r}{\partial x} \\ hK_r\frac{\partial h_r}{\partial y} \end{pmatrix},$$

where $\mathbf{w}$ is the vector of conserved variables, F_x and F_y are the two components of the momentum flux, $\mathbf{S}$ is the bed slope source term, $\mathbf{T}$ is the total friction term, and $\mathbf{P}$ is the new surface pressure term. According to Equation (8), in regions where the water depth is lower than the roof height $h_r = h$, and therefore all the terms including K_r in Equation (19) cancel each other, recovering the standard shallow water equations.

A first order in time, explicit, unstructured finite volume discretization of Equation (19) in a cell-centered control volume (Figure 2) is given by:

$$\frac{\mathbf{w}_i^{n+1} - \mathbf{w}_i^n}{\Delta t} A_i + \sum_{j \in N_i} \int_{L_{ij}} (\mathbf{F_x} n_x + \mathbf{F_y} n_y)_{ij}^n \, dL = \int_{A_i} \mathbf{H}^n \, dA,$$

(20)

where the superindex n refers to time t^n, $\mathbf{H} = \mathbf{S} + \mathbf{T} + \mathbf{P}$ accounts for all the source terms, $\mathbf{w}_i^n$ is an approximation of the average value of $\mathbf{w}$ in the control volume C_i at time t^n, A_i is the area of the control volume C_i, L_{ij} is the length of the common face to the volumes C_i and C_j, $\mathbf{n} = (n_x, n_y)$ is a unit vector perpendicular to the cell face and pointing from C_i to C_j, and N_i denotes all the volumes C_j that share any face with the volume C_i.

The integral of the momentum flux in Equation (20) is approximated at each finite volume face by the so-called numerical flux $\mathbf{\Phi}_{ij}$ as:

$$\sum_{j \in N_i} \int_{L_{ij}} (\mathbf{F_x} n_x + \mathbf{F_y} n_y) \, dL \approx \mathbf{\Phi}_i = \sum_{j \in N_i} \mathbf{\Phi}_{ij} L_{ij}.$$

(21)
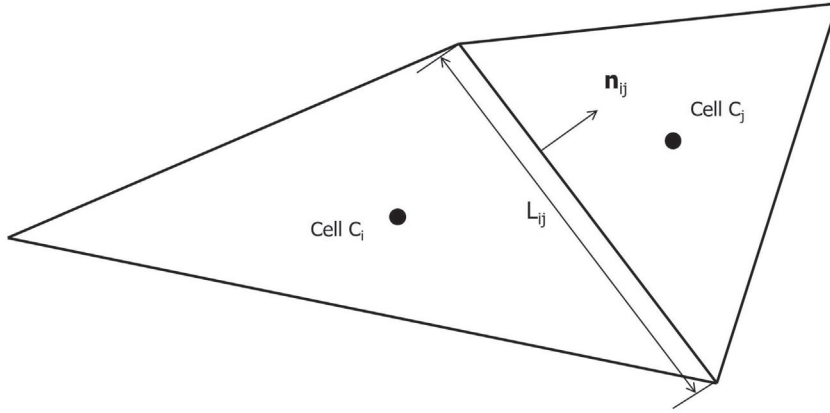
FIGURE 2 Sketch of the unstructured finite-volume discretization used in the solver, showing the geometric variables used to compute the flux between cells C_i and C_j

In this study we have used a first-order discretization of the numerical flux, although higher order schemes could be introduced in the evaluation of $\mathbf{\Phi}_{ij}$ in order to increase the spatial accuracy of the numerical discretization. The numerical flux in Equation (21) is split in a centered $\mathbf{\Phi}_{ij}^C$ and an upwind contribution $\mathbf{\Phi}_{ij}^U$, which are computed in terms of the eigenvectors $\tilde{\mathbf{e}}_m$ and eigenvalues $\tilde{\lambda}_m$ of the Jacobian matrix of the normal flux as[46]:

$$\mathbf{\Phi}_{ij} = \mathbf{\Phi}_{ij}^C + \mathbf{\Phi}_{ij}^U \quad \mathbf{\Phi}_{ij}^C = \left(\frac{\mathbf{Z}_i + \mathbf{Z}_j}{2}\right) \quad \mathbf{\Phi}_{ij}^U = \left(-\frac{1}{2}\sum_{m=1}^{3}|\tilde{\lambda}_m|\alpha_m\tilde{\mathbf{e}}_m\right), \tag{22}$$

where $\mathbf{Z} = F_x n_x + F_y n_y$ is the normal flux to the cell face. The eigenvalues $\tilde{\lambda}_m$ and eigenvectors $\tilde{\mathbf{e}}_m$ are given by:

$$\tilde{\lambda}_1 = \tilde{\lambda}_2 + \tilde{c} \quad \tilde{\lambda}_2 = n_x\tilde{U}_x + n_y\tilde{U}_y \quad \tilde{\lambda}_3 = \tilde{\lambda}_2 - \tilde{c}, \tag{23}$$

$$\tilde{\mathbf{e}}_1 = \begin{pmatrix} 1 \\ \tilde{U}_x + \tilde{c}n_x \\ \tilde{U}_y + \tilde{c}n_y \end{pmatrix} \quad \tilde{\mathbf{e}}_2 = \begin{pmatrix} 0 \\ -\tilde{c}n_y \\ \tilde{c}n_x \end{pmatrix} \quad \tilde{\mathbf{e}}_3 = \begin{pmatrix} 1 \\ \tilde{U}_x - \tilde{c}n_x \\ \tilde{U}_y - \tilde{c}n_y \end{pmatrix}.$$

The eigenvectors $\tilde{\mathbf{e}}_m$ and the eigenvalues $\tilde{\lambda}_m$ are evaluated at the mean state of Roe, which is given by[51]:

$$\tilde{h} = \sqrt{h_i h_j} \quad \tilde{c} = \sqrt{(g + K_{r,ij}^*)\frac{h_i + h_j}{2}}$$

$$\tilde{U}_x = \frac{\sqrt{h_i}U_{x,i} + \sqrt{h_j}U_{x,j}}{\sqrt{h_i} + \sqrt{h_j}} \quad \tilde{U}_y = \frac{\sqrt{h_i}U_{y,i} + \sqrt{h_j}U_{y,j}}{\sqrt{h_i} + \sqrt{h_j}} \tag{24}$$

with:

$$K_{r,ij}^* = \begin{cases} 0 & \text{if } h_i \leq z_{r,i} - z_{b,i} \quad \text{and} \quad h_j \leq z_{r,j} - z_{b,j} \\ K_r & \text{if } h_i > z_{r,i} - z_{b,i} \quad \text{or} \quad h_j > z_{r,j} - z_{b,j} \end{cases}. \tag{25}$$

The previous definition of $\tilde{c}$ takes into account the increase in wave celerity in pressurized flow conditions ($h > z_r - z_b$), and recovers the standard shallow water celerity under free surface conditions ($h \leq z_r - z_b$). At the cell edges located at the transitions between free surface and pressurized flow (i.e., when just one of the adjacent elements to the cell face is under pressure), the wave celerity under pressurized conditions is considered.

The expression for the coefficients α_m in Equations (22) is given by[46]:

$$\alpha_{1,3} = \frac{h_j - h_i}{2} \pm \frac{1}{2\tilde{c}}[(U_{x,j}h_j - U_{x,i}h_i)n_x + (U_{y,j}h_j - U_{y,i}h_i)n_y - (\tilde{U}_x\tilde{n}_x + \tilde{U}_y n_y)(h_j - h_i)], \tag{26}$$

$$\alpha_2 = \frac{1}{\tilde{c}}[(U_{y,j}h_j - U_{y,i}h_i - \tilde{U}_y(h_j - h_i))n_x - (U_{x,j}h_j - U_{x,i}h_i - \tilde{U}_x(h_j - h_i))n_y].$$

The bed slope term is discretized with the upwind scheme described in previous studies, such as References 47 and 52, and is based on the upwind scheme originally presented in References 44 for the standard 2D-SWE. Using the Gauss theorem, the surface integral of the bed slope term over a finite volume cell can be written as:

$$\int_{C_i} \mathbf{S} dA \approx \mathbf{S_i} = \sum_{j \in N_i} \mathbf{S_{ij}} L_{ij} \quad \mathbf{S_{ij}} = \mathbf{S_{ij}}^C + \mathbf{S_{ij}}^U, \tag{27}$$

$$\mathbf{S_{ij}}^C = \sum_{m=1}^{3} \beta_m^C \tilde{\mathbf{e}}_m \quad \mathbf{S_{ij}}^U = \sum_{m=1}^{3} \beta_m^U \tilde{\mathbf{e}}_m,$$

where the superindices C and U refer respectively to the centered and upwind contributions in the source term discretization. The coefficients β_m^C, β_m^U are given by:

$$\beta_1^C = -\frac{1}{4} \frac{g}{\tilde{c}_{ij}} h_{ij} \Delta z_{b,ij} \quad \beta_1^U = \text{sgn}(\tilde{\lambda}_1) \frac{1}{4} \frac{g}{\tilde{c}_{ij}} h_{ij} \Delta z_{b,ij},$$

$$\beta_2^C = 0 \qquad\qquad \beta_2^U = 0, \tag{28}$$

$$\beta_3^C = \frac{1}{4} \frac{g}{\tilde{c}_{ij}} h_{ij} \Delta z_{b,ij} \quad \beta_3^U = -\text{sgn}(\tilde{\lambda}_3) \frac{1}{4} \frac{g}{\tilde{c}_{ij}} h_{ij} \Delta z_{b,ij},$$

where $h_{ij} = \frac{h_i + h_j}{2}$ and $\Delta z_{b,ij} = z_{b,j} - z_{b,i}$.

The new source term $\mathbf{P}$ in Equation (19) is discretized following a similar scheme as for the bed slope term:

$$\int_{C_i} \mathbf{P} dA \approx \mathbf{P_i} = \sum_{j \in N_i} \mathbf{P_{ij}} L_{ij} \quad \mathbf{P_{ij}} = \mathbf{P_{ij}}^C + \mathbf{P_{ij}}^U, \tag{29}$$

$$\mathbf{P_{ij}}^C = \sum_{m=1}^{3} \gamma_m^C \tilde{\mathbf{e}}_m \quad \mathbf{P_{ij}}^U = \sum_{m=1}^{3} \gamma_m^U \tilde{\mathbf{e}}_m,$$

where the superindices C and U refer respectively to the centered and upwind contributions. Considering the similarity between the source terms $\mathbf{S}$ and $\mathbf{P}$, the coefficients γ_m^C, γ_m^U are given by:

$$\gamma_1^C = \frac{1}{4} \frac{K_r}{\tilde{c}_{ij}} h_{ij} \Delta h_{r_{ij}} \quad \gamma_1^U = -\text{sgn}(\tilde{\lambda}_1) \frac{1}{4} \frac{K_{r,ij}^*}{\tilde{c}_{ij}} h_{ij} \Delta h_{r_{ij}}$$

$$\gamma_2^C = 0 \quad \gamma_2^U = 0$$

$$\gamma_3^C = -\frac{1}{4} \frac{K_r}{\tilde{c}_{ij}} h_{ij} \Delta h_{r_{ij}} \quad \gamma_3^U = \text{sgn}(\tilde{\lambda}_3) \frac{1}{4} \frac{K_{r,ij}^*}{\tilde{c}_{ij}} h_{ij} \Delta h_{r_{ij}}, \tag{30}$$

where $h_{ij} = \frac{h_i + h_j}{2}$, $\Delta h_{r_{ij}} = h_{r,j} - h_{r,i}$, and h_r is defined by Equation (8). Notice that the coefficients γ_m^C are computed using the roof stiffness constant K_r, while the coefficients γ_m^U are computed with $K_{r,ij}^*$ as defined in Equation (25). As will be shown in following sections, this is necessary in order to recover an exact balance in the mass and momentum equations under hydrostatic conditions.

3.2 | Numerical stability

The computational time step in Equation (20) is limited by the Courant–Friedrichs–Lewy (CFL) stability constraint.[43] Various slightly different definitions of the CFL condition have been used in unstructured solvers for the 2D-SWE, which differ mainly in the definition of the characteristic length of a grid cell.[48-50,53] In the solver used in the current study, the computational time step is defined as:

$$\Delta t = \min \Delta t_i \quad i = 1, M \quad \Delta t_i = \text{CFL} \frac{\min_{j \in N_i} L_{ij}}{|\mathbf{U}|_i + c_w}, \tag{31}$$

where $|\mathbf{U}|_i$ is the modulus of the water velocity in the finite volume C_i, L_{ij} is the length of the cell face which joins the control volumes C_i and C_j, N_i are all the control volumes C_j which share any face with C_i, M is the number of cells in the mesh, and c_w is the wave celerity. For numerical stability the CFL must be lower than 1 in 1D problems and lower than 0.5 in 2D meshes. The wave celerity is equal to $c_w = \sqrt{(g + K_r)h}$ in mesh elements under pressurized conditions ($h > z_r - z_b$) and $c_w = \sqrt{gh}$ in free surface elements ($h \leq z_r - z_b$).

3.3 | Analysis of the C-property: Hydrostatic conditions

A usual requirement is that a numerical solver for the shallow water equations satisfies the so-called C-property, presented originally by Bertin et al.[54] According to this property, the numerical scheme must be able to reproduce exactly the hydrostatic condition (water at rest). Under hydrostatic conditions ($q_x = q_y = 0$), the proposed x-momentum equation reduces to:

$$g\frac{\partial h}{\partial x} = -g\frac{\partial z_b}{\partial x} - K_r \frac{\partial}{\partial x}(h - h_r). \tag{32}$$

Rearranging terms, Equation (32) can be written in a discrete form as:

$$K_r \Delta h_r = (g + K_r)\Delta h + g\Delta z_b. \tag{33}$$

In order to satisfy the C-property, the discretization scheme must satisfy Equation (33) under hydrostatic conditions. Note that in free surface regions $h_r = h$ (from Equation 8), and thus Equation (33) reduces to $\Delta h = -\Delta z_b$, which implies a constant free surface elevation.

When water is at rest, the momentum fluxes and source terms in Equations (19) reduce to:

$$\mathbf{F_x} = \begin{pmatrix} 0 \\ \frac{(g+K_r)h^2}{2} \\ 0 \end{pmatrix} \quad \mathbf{F_y} = \begin{pmatrix} 0 \\ 0 \\ \frac{(g+K_r)h^2}{2} \end{pmatrix},$$

$$\mathbf{S} = \begin{pmatrix} 0 \\ -gh\frac{\partial z_b}{\partial x} \\ -gh\frac{\partial z_b}{\partial y} \end{pmatrix} \quad \mathbf{T} = \begin{pmatrix} 0 \\ 0 \\ 0 \end{pmatrix} \quad \mathbf{P} = \begin{pmatrix} 0 \\ hK_r\frac{\partial h_r}{\partial x} \\ hK_r\frac{\partial h_r}{\partial y} \end{pmatrix}.$$

The numerical flux defined in Equation (21) is therefore given by:

$$\boldsymbol{\Phi}_i = \sum_{j\in N_i}\boldsymbol{\Phi}_{ij}L_{ij} = \sum_{j\in N_i}\frac{L_{ij}}{2}\left[\underbrace{(g+K_r)\frac{h_i^2+h_j^2}{2}\begin{pmatrix}0\\n_{x,ij}\\n_{y,ij}\end{pmatrix}}_{\text{centered}} - \underbrace{\tilde{c}\Delta h_{ij}\begin{pmatrix}1\\0\\0\end{pmatrix}}_{\text{upwind}}\right]. \tag{34}$$

While the source terms $\boldsymbol{P}_i$ and $\boldsymbol{S}_i$ can be written as:

$$\mathbf{S}_i = \sum_{j\in N_i}\mathbf{S}_{ij}L_{ij} = \sum_{j\in N_i}\frac{|\mathbf{n}_{ij}|}{2}gh_{ij}\Delta z_{b,ij}\left[\underbrace{-\begin{pmatrix}0\\n_{x,ij}\\n_{y,ij}\end{pmatrix}}_{\text{centered}} + \underbrace{\frac{1}{\tilde{c}}\begin{pmatrix}1\\0\\0\end{pmatrix}}_{\text{upwind}}\right], \tag{35}$$

$$\mathbf{P}_i = \sum_{j \in K_i} \mathbf{P}_{ij} L_{ij} = \sum_{j \in K_i} \frac{L_{ij}}{2} h_{ij} \Delta h_{r,ij} \left[K_r \underbrace{\begin{pmatrix} 0 \\ n_{x,ij} \\ n_{y,ij} \end{pmatrix}}_{\text{centered}} - \underbrace{\frac{K^*_{r,ij}}{\tilde{c}} \begin{pmatrix} 1 \\ 0 \\ 0 \end{pmatrix}}_{\text{upwind}} \right]. \tag{36}$$

We will show first that the upwind contributions of $\mathbf{\Phi}_i$, $\mathbf{S}_i$, and $\mathbf{P}_i$ are exactly balanced. The upwind residual ($\mathbf{R}^U_i$) computed from the upwind contributions of $\mathbf{\Phi}_i$, $\mathbf{S}_i$ and $\mathbf{P}_i$ equals:

$$\mathbf{R}^U_i = \sum_{j \in N_i} \mathbf{R}^U_{ij} L_{ij} = \sum_{j \in N_i} L_{ij} (\mathbf{\Phi}^U_{ij} - \mathbf{S}^U_{ij} - \mathbf{P}^U_{ij}) \tag{37}$$

$$= \sum_{j \in N_i} \frac{L_{ij}}{2} \left(-\tilde{c} \Delta h_{ij} - \frac{g h_{ij}}{\tilde{c}} \Delta z_{b,ij} + h_{ij} \Delta h_{r,ij} \frac{K^*_{r,ij}}{\tilde{c}} \right) \begin{pmatrix} 1 \\ 0 \\ 0 \end{pmatrix}.$$

At free surface edges, $\tilde{c} = \sqrt{g h_{ij}}$ and $K^*_{r,ij} = 0$ (from Equation 25). Bearing in mind that under hydrostatic conditions $\Delta h_{ij} = -\Delta z_{b,ij}$, it is straightforward to show that $\mathbf{R}^U_{ij} = 0$ at every finite volume edge, and thus $\mathbf{R}^U_i = 0$.

At pressurized edges, it follows from Equation (25) that $K^*_{r,ij} = K_r$ and $\tilde{c} = \sqrt{(g + K_r) h_{ij}}$. Using Equation (33) and simple mathematical manipulation, it is straightforward to show that the upwind contributions in Equations (37) balance each other exactly and thus, $\mathbf{R}^U_{ij} = 0$ at every finite volume edge also under pressurized conditions.

Regarding the centered contributions, using Equation (33), the following residual is obtained when comparing the terms $\mathbf{\Phi}_i$, $\mathbf{S}_i$, and $\mathbf{P}_i$:

$$\mathbf{R}^C_i = \sum_{j \in N_i} \frac{L_{ij}}{2} (g + K_r) h_i^2 \begin{pmatrix} 0 \\ n_{x,ij} \\ n_{y,ij} \end{pmatrix}. \tag{38}$$

Since K_r and g are both constant, the residual $\mathbf{R}^C_i$ equals:

$$\mathbf{R}^C_i = \frac{(g + K_r)}{2} h_i^2 \sum_{j \in N_i} L_{ij} \begin{pmatrix} 0 \\ n_{x,ij} \\ n_{y,ij} \end{pmatrix}. \tag{39}$$

The balance of the centered contributions ($\mathbf{R}^C_i = 0$) follows directly by simply considering that for any closed volume the following relation applies for both the x and the y component of the normal vector:

$$\sum_{j \in N_i} h_i^2 n_{x,ij} L_{ij} = h_i^2 \sum_{j \in N_i} n_{x,ij} L_{ij} = 0. \tag{40}$$

4 | RESULTS AND DISCUSSION

In this section we analyze the performance of the proposed model in several test cases. In test case T1 the numerical stability of the proposed scheme and its ability to maintain the hydrostatic condition (C-property) is shown. In the second test case (T2) the proposed formulation is compared with a standard solver for the shallow water equations, in order to show that both solvers give exactly the same solution when the water elevation does not reach the roof. Test case T3 compares the numerical results to an analytical solution in a 1D channel under mixed flow conditions. The fourth test case (T4) is a 2D circular dam-break problem partially confined in the vertical direction by a roof. The model results are
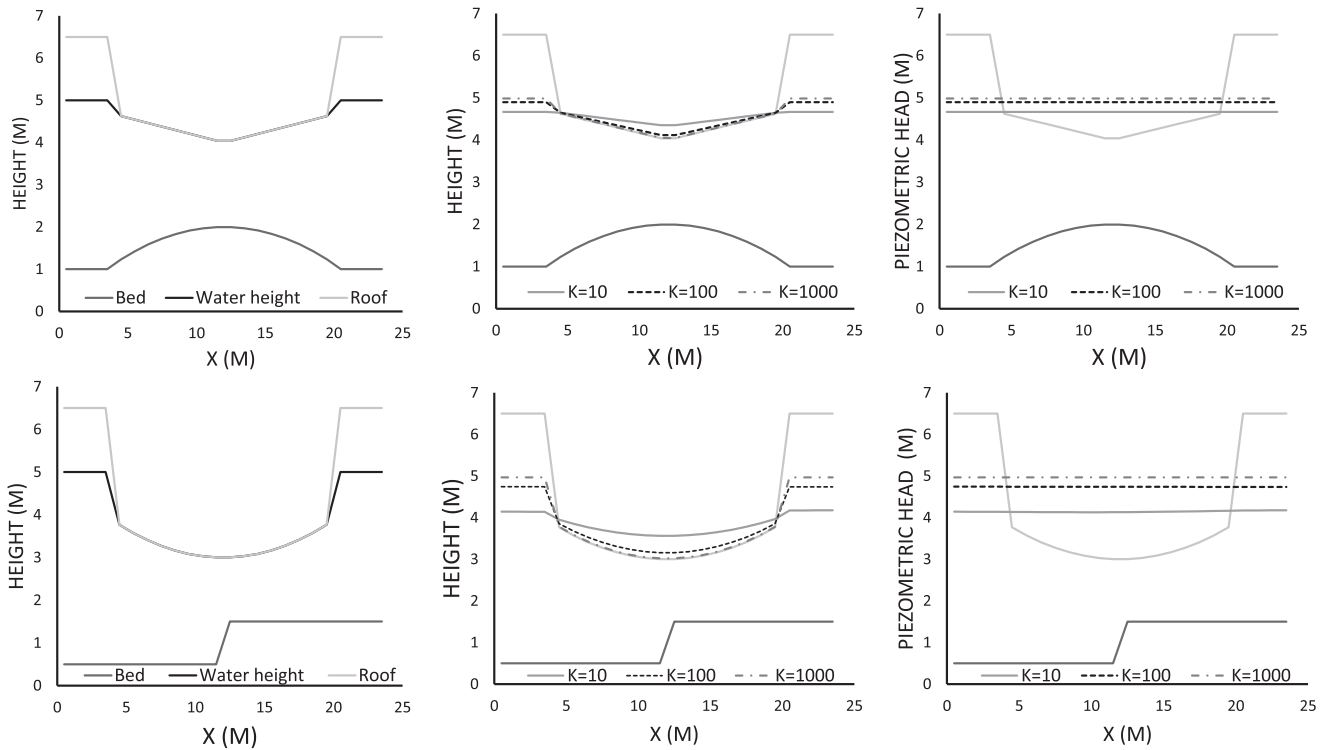
FIGURE 3 Test case T1. Initial water depth (left), water surface ($z_b + h$) (center), and piezometric head (right), for two different channel geometries [Colour figure can be viewed at wileyonlinelibrary.com]

compared with a reference solution obtained numerically by Maranzoni et al.[18] using an approach completely different from the one proposed in this study. Test case T5 consists of a channel junction under partially pressurized conditions, and is used to show the capability of the model to handle 2D configurations. Finally, test cases T6 and T7 correspond to flows under partially submerged bridges. In both tests the numerical results obtained with the proposed methodology are compared against experimental data from Reference 12.

4.1 | Test case T1: Hydrostatic conditions

This test case serves several purposes: (1) to prove the mass conservation property of the numerical solver; (2) to show the effect that the value of the stiffness constant K_r has on the accuracy of the numerical results; (3) to prove that the scheme is stable and fulfills the C-property.

A 24-m long 1D channel with two different bed and roof geometries is considered. In the first configuration the channel has a curved bed and a triangular roof, while the second configuration has a piecewise constant bed and a curved roof (Figure 3). All the boundaries are walls, that is, there is no flow into or out of the domain. The mesh resolution of the numerical method is 1 m. Both cases are solved numerically with different values of the stiffness constant, ranging from 10 to 1000 m/s^2 (Table 1).

The initial water velocity is zero, and the water height corresponds to a hydrostatic state with a water elevation of 5 m outside the roof. Inside the roof the initial water elevation is equal to the roof elevation. Thus, the initial water depth at each node (h_i^0) is defined by:

$$h_i^0 = \min(5, z_{r,i} - z_{b,i}) \quad i = 1, M, \tag{41}$$

where M is the number of mesh elements. As discussed in previous sections, the proposed formulation introduces a certain degree of elasticity in the roof (which depends on the value of K_r). Thus, even though the initial condition corresponds to an exact hydrostatic state, in the numerical simulation the water depth inside the roof will

TABLE 1 Test case T1

K_r (m/s²)	Initial water mass (m³)	Final water mass (m³)	Max CFL	Error
Triangular roof, circular bed				
10	73.96	73.96	0.9	0.0768
100	73.96	73.96	0.9	0.0202
1000	73.96	73.96	0.9	0.0025
Circular roof, piecewise constant bed				
10	68.62	68.62	0.9	0.1860
100	68.62	68.62	0.9	0.0524
1000	68.62	68.62	0.9	0.0065

Note: Maximum relative error (MRE), as defined by Equation (42), and maximum CFL needed to achieve numerical stability for different values of the stiffness constant. Columns 2 and 3 show the water mass in the system (m³) and vouch for the conservation property of the numerical scheme.

increase slightly before achieving a new steady state, in which the C-property is preserved. At the same time, the water depth outside the roof will decrease in order to fulfill the mass conservation property. The difference between the water depths in the final and initial steady states will depend on the value of K_r, and will determine the accuracy of the solution. But no matter the value of K_r used, a hydrostatic steady solution without any spurious oscillations is always obtained. To this end, the maximum relative error (MRE) of the numerical solution is defined as the maximum difference between the computed steady-state water height (h_i) and the initial water depth (h_i^0), and is given by:

$$\mathrm{MRE} = \max_{i=1,\,\ldots,\,M} \frac{|h_i - h_i^0|}{h_i^0}. \tag{42}$$

Table 1 shows the MRE of the numerical solution obtained with the proposed discretization in combination with different values of K_r. The error tends to zero as the value of K_r increases, meaning that the numerical scheme is consistent. The error is highly dependent on the value of K_r, because this parameter controls the elasticity of the roof. In the cases analyzed here, a value of $K_r = 10$ m/s² produces relative errors on the water depth up to 18%, while the MRE diminishes below 1% when $K_r = 1000$ m/s². It is also worth noting that numerical stability is achieved with a value of CFL $= 0.9$ independently of the value of K_r.

## 4.2 | Test case T2: Dam break with no roof pressure

This test case is used to show that the proposed formulation gives the same results as a standard 2D-SWE solver under free surface conditions. It also serves to verify that, under free surface conditions the discretization of the new pressure term added to the momentum fluxes in Equations (14–15) is well balanced and consistent with the discretization of the new source term including K_r. The test case consists of a 24-m long 1D channel with closed boundaries (no flux inside or outside the domain) and a roof located high enough so that it does not influence the water flow. The channel is discretized with a structured mesh with a spatial resolution of 0.5 m. A dam is located at the center of the channel, with an initial water depth of 2 m to the left and 0.5 m to the right. The Manning coefficient is set to $n = 0.010$ s/m$^{1/3}$. The results of this test case are independent of K_r since the water does not reach the roof. To verify this, the test has been run for different values of the stiffness constant ranging from $K_r = 10$ m/s² to $K_r = 1000$ m/s², although the comparison is not shown here because the results are exactly the same.

Figure 4 shows the comparison between the standard 2D-SWE solver and the results obtained with the proposed formulation at four different times. As can be observed, the numerical solutions obtained with the standard solver and the proposed discretization are virtually the same.
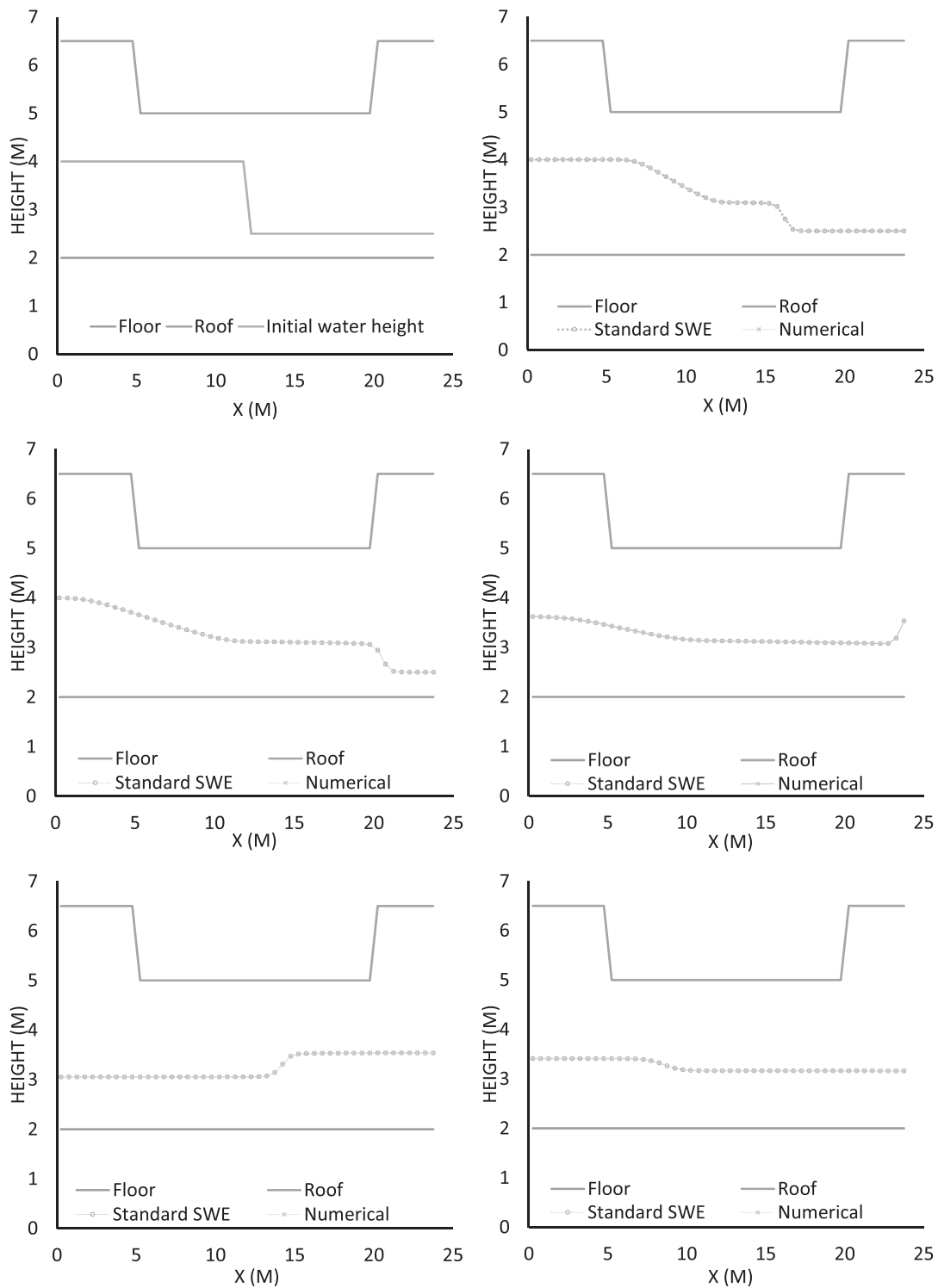
FIGURE 4 Test case T2. Water elevation profiles at $t = 0$ s (upper left), $t = 1$ s (upper right), $t = 2$ s (middle left), $t = 3$ s (middle right), $t = 20$ s (bottom left), and $t = 40$ s (bottom right). Gray dots represent the solution obtained with the standard 2D-SWE solver, whereas yellow crosses are the results obtained with the proposed formulation [Colour figure can be viewed at wileyonlinelibrary.com]

FIGURE 5 Test case T3. Numerical profiles of piezometric head for different values of the stiffness constant [Colour figure can be viewed at wileyonlinelibrary.com]
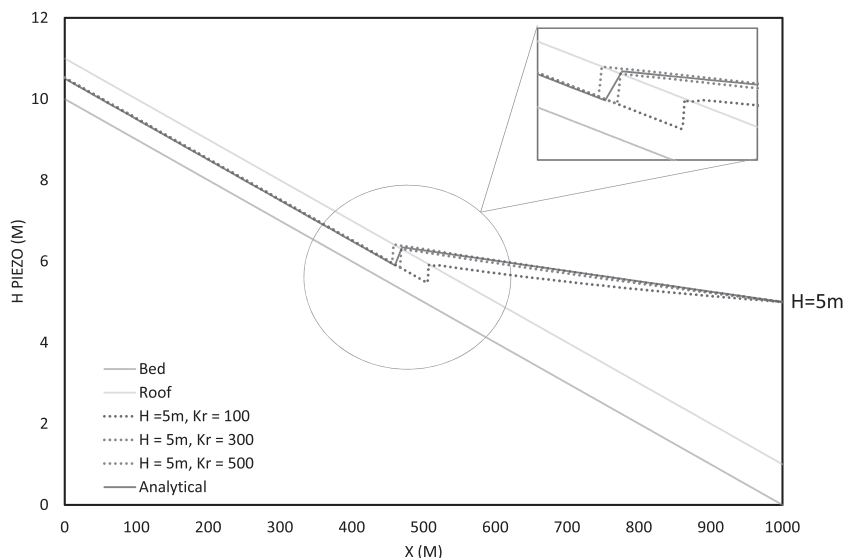
4.3 | Test case T3: Steady mixed flow in a 1D channel

This test case is very similar to one of the cases employed by Malekpour and Karney[17] to test a 1D mixed flow solver that uses the Preissmann slot method to account for pressurized conditions. It consists of a 1000-m long 1D channel with a constant slope of 1% and a square cross-section of 1 m height and 1 m width. The flow conditions are steady, with a discharge of 2 m³/s imposed at the inlet boundary. The inlet boundary condition is imposed in terms of the water velocity and water depth corresponding to uniform flow conditions with a Manning coefficient of $n = 0.010 \, \text{s/m}^{1/3}$ (inlet velocity of 3.976 m/s and water depth of 0.503 m). At the downstream outlet boundary the piezometric head is imposed in order to assure submerged conditions at the end of the channel.

Under the previous conditions the flow at the channel inlet is supercritical with a Froude number of 1.79. At some point in the channel, the location of which depends on the value of the piezometric head imposed at the outlet boundary, an hydraulic jump occurs and the flow becomes pressurized immediately after this hydraulic jump, that is, one of the conjugate states corresponds to a free surface flow and the other to a pressurized flow. Even if the geometry is 1D, this test case is very challenging due to the sudden transition between free surface and pressurized conditions through an hydraulic jump. At the same time, the position of the hydraulic jump is very sensitive to the Manning coefficient and therefore, to the discretization of the bed friction.

The analytic solution for this test case can be easily obtained. It consists of two flow states defined by uniform open channel flow and uniform pressurized flow, separated by a hydraulic jump. Since uniform conditions occur upstream and downstream of the hydraulic jump, the head loss and momentum flux can be computed exactly for each channel reach. The location of the hydraulic jump can be analytically computed as the point at which the momentum flux in both reaches is the same.

In the numerical model the channel is discretized using quadrilateral elements with a mesh resolution of 0.5 m. Since the geometry is 1D, only one element is used in the transverse direction. Figure 5 shows the effect of the stiffness constant on the solution for the case in which the piezometric head at the downstream boundary is fixed to 5 m. Small values of K_r (such as $K_r = 100 \, \text{m/s}^2$) produce a greater difference between the analytical solution and the numerical one, causing the hydraulic jump to move downstream. With higher values of K_r, we are able to obtain solutions that are much closer to the analytical solution, but the computational cost increases as high values of K_r mean smaller values of the CFL number and, therefore, larger simulation times. Note that the analytical solution is obtained considering a completely rigid roof, and thus it corresponds to a value of $K_r \to \infty$.

For comparison with the analytical solution, the stiffness constant was set to $K_r = 300 \, \text{m/s}^2$ which, according to Figure 5, is considered to be a good compromise between accuracy and computational efficiency, and the value of the CFL was set to 0.9. The piezometric head profiles predicted by the numerical model are compared with the analytic solution for several values of the downstream boundary condition in Figure 6. The model represents properly the pressurized flow conditions and the dependence of the hydraulic jump position on the downstream boundary condition. The sharp
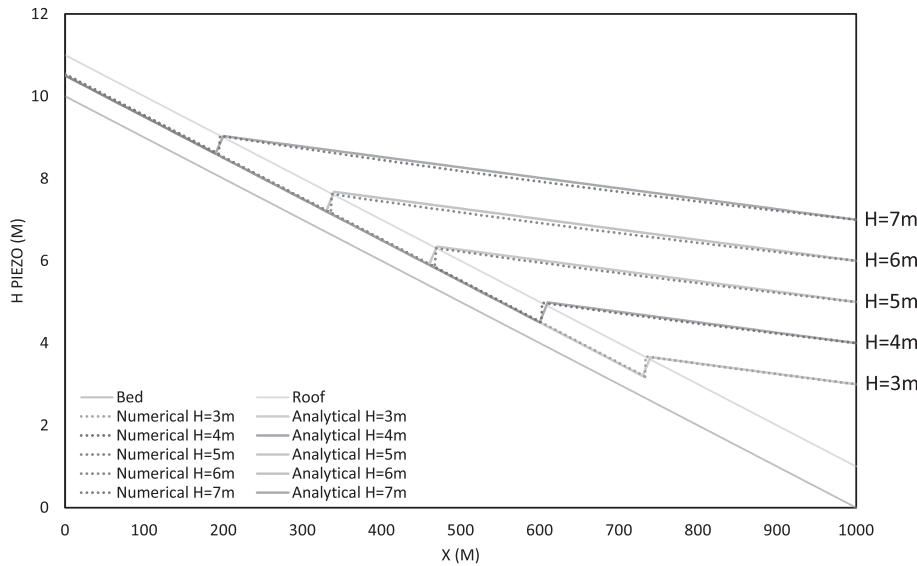
FIGURE 6 Test case T3. Analytic and numerical profiles of piezometric head for different downstream boundary conditions [Colour figure can be viewed at wileyonlinelibrary.com]

transition between free surface supercritical flow and pressurized subcritical flow is resolved by the scheme without numerical instabilities.

4.4 | Test case T4: 2D circular dam-break under a roof

This test case was used by Maranzoni et al.[18] to validate an extension of the Preissmann slot method to 2D transient mixed flows. It consists of a circular dam-break over a flat bed with a 5-m high ceiling. Both the bed and the ceiling are frictionless. At the beginning of the simulation a pressurized water column with a piezometric head of 10 m and a radius of 11 m is placed in the center of the spatial domain. In the rest of the domain the initial water depth is 1 m. As explained in Reference 18, the sudden release of the pressurized water column generates a transitional rarefaction moving toward the center of the water column and a free surface shock wave moving away (Figure 7).

In order to solve the problem with the proposed formulation, a rectangular domain of 25×25 m was discretized with a mesh resolution of 5 cm. As explained in previous sections, the celerity of the pressurized wave depends on the stiffness constant K_r. Figure 8 shows the effect of the stiffness constant on the solution, for values of K_r ranging from 10 to 1000 m/s². The wave celerity under pressurized conditions is very sensitive to K_r. However, when the flow becomes depressurized, the difference between the solution obtained with $K_r = 450$ m/s² and $K_r = 1000$ m/s² is relatively small. On the other hand, a value of $K_r = 10$ m/s² gives very different results at all times.

Here, we will evaluate the performance of the proposed model against the reference solution presented in Reference 18, which was obtained by solving numerically a 1D radial equation for mixed flow conditions in a very fine mesh, with a spatial resolution of 0.625 cm (i.e., approximately 10 times finer than the mesh used to solve the test case with the proposed formulation). Therefore, the reference solution is not an analytical solution to the problem, but simply a numerical approximation computed with a pressurized wave celerity of approximately 50 m/s. In order to reproduce the same wave celerity with which the test case was solved in Reference 18, the stiffness constant in the proposed formulation was set to $K_r = 450$ m/s² which, considering a ceiling height of 5 m, gives a pressurized wave celerity of $c = \sqrt{(g + K_r)h} = 48$ m/s. Figure 7 shows the time evolution of the piezometric head computed with the proposed formulation. Since the mesh is 2D, the CFL is set to 0.5.

Figure 9 compares the piezometric head computed at different times with the proposed model against the reference solution by Maranzoni et al.[18] It can be observed that the proposed scheme reproduces the same behavior as the reference solution. The solution obtained at $t = 0.1$ s with the proposed scheme gives a smoother definition of the pressurized wave ($x = 6$ m) than the reference solution, which gives a sharper wave front. Nevertheless, when comparing the results it should be borne in mind that the mesh size used to compute the reference solution was 10 times finer. Otherwise, the scheme predicts the same results as the reference solution of Maranzoni et al.[18]
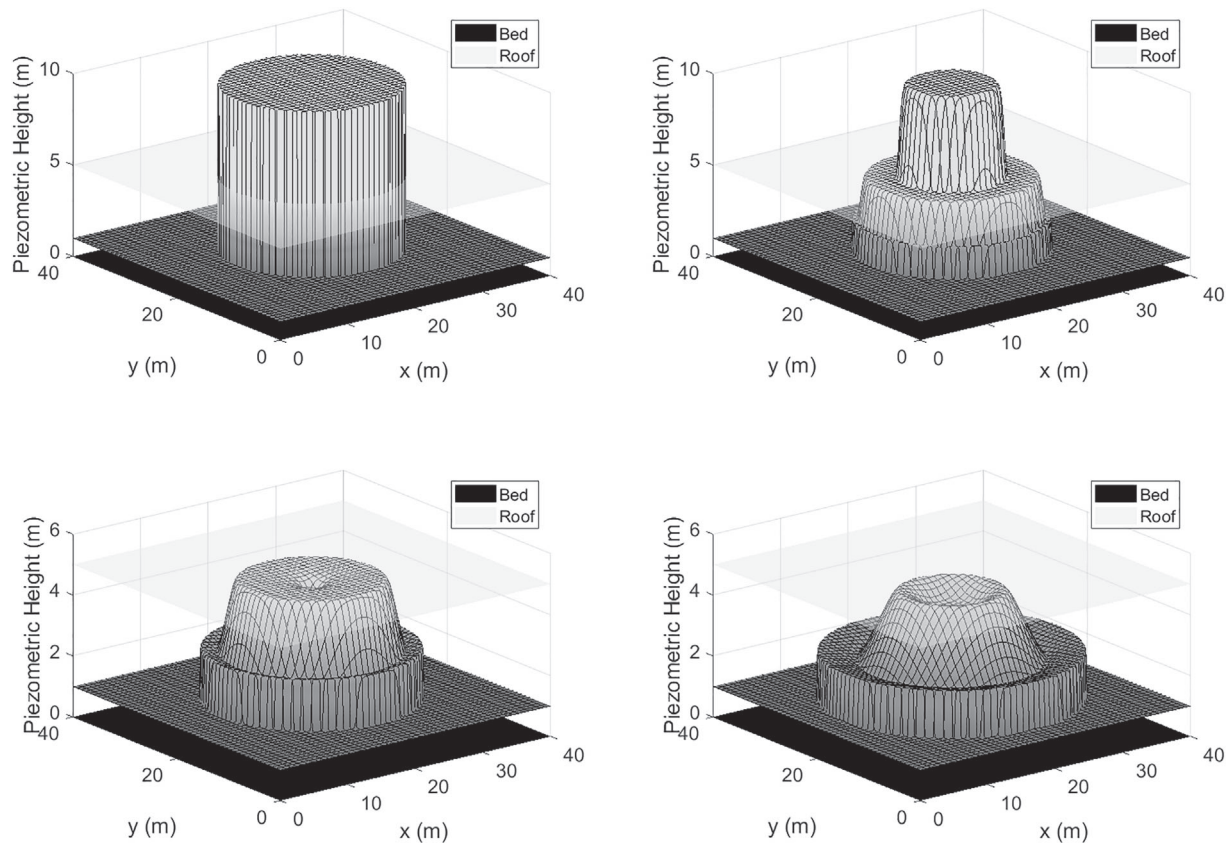
FIGURE 7 Test case T4. 3D images of the piezometric head at four different times: $t = 0$ s (upper left); $t = 0.1$ s (upper right); $t = 0.3$ s (lower left); $t = 0.7$ s (lower right) [Colour figure can be viewed at wileyonlinelibrary.com]

4.5 | Test case T5: Channel junction

This test case consists of a channel junction at a 90° angle (Figure 10). Both channels have a rectangular cross-section, 4 m wide and 2 m high, and a Manning coefficient of $n = 0.016$ s/m$^{1/3}$. The bed slope is 0.1% in the main channel and 1% in the tributary channel. The main channel length is 35 m, while the tributary has a length of 10 m. The boundary conditions are the piezometric head at the main channel outlet and the water discharge at the two channel inlets. Several combinations of the inlet water discharge and the outlet piezometric head have been modeled in order to achieve different pressurized conditions in the channels (see Figure 11). The channel geometry is discretized with a structured mesh with a spatial resolution of 20 cm (Figure 10, upper left). Since the mesh is 2D, in order to obtain stable results the test case is solved with a CFL value of 0.5. No reference solution is available for this test case, so the analysis of the results is limited to the comparison of the solutions obtained with different boundary conditions and on the stability of the scheme.

Figure 10 shows the results obtained with the proposed formulation, with a total inlet discharge of 20 m^3/s (10 m^3/s through each inlet) and an outlet piezometric head of 1.80 m. Under these conditions, pressurized flow occurs at the junction and upstream of the junction. Downstream of the junction the flow becomes supercritical and a hydraulic jump occurs. A longitudinal profile of the water depth and piezometric head along the center line of the main channel for these boundary conditions is shown in Figure 11 (upper right). It is worth noting how the water depth fits the roof height in the pressurized region (from $x = 20$ m to $x = 30$ m). The small differences are due to the elasticity of the roof introduced in the equations, with a value for the stiffness constant of $K_r = 300$ m/s^2. The effect of the roof on the piezometric head is shown in the bottom-right panel of Figure 11, which shows the longitudinal profiles of piezometric head along the center line of the main channel with and without roof. The head loss between the inlet and outlet of the main channel increases by about 0.7 m when the roof is introduced, mainly due to the higher water velocity in the vertically constrained section, which in turn induces a hydraulic jump at $x = 11$m in the case with the roof.
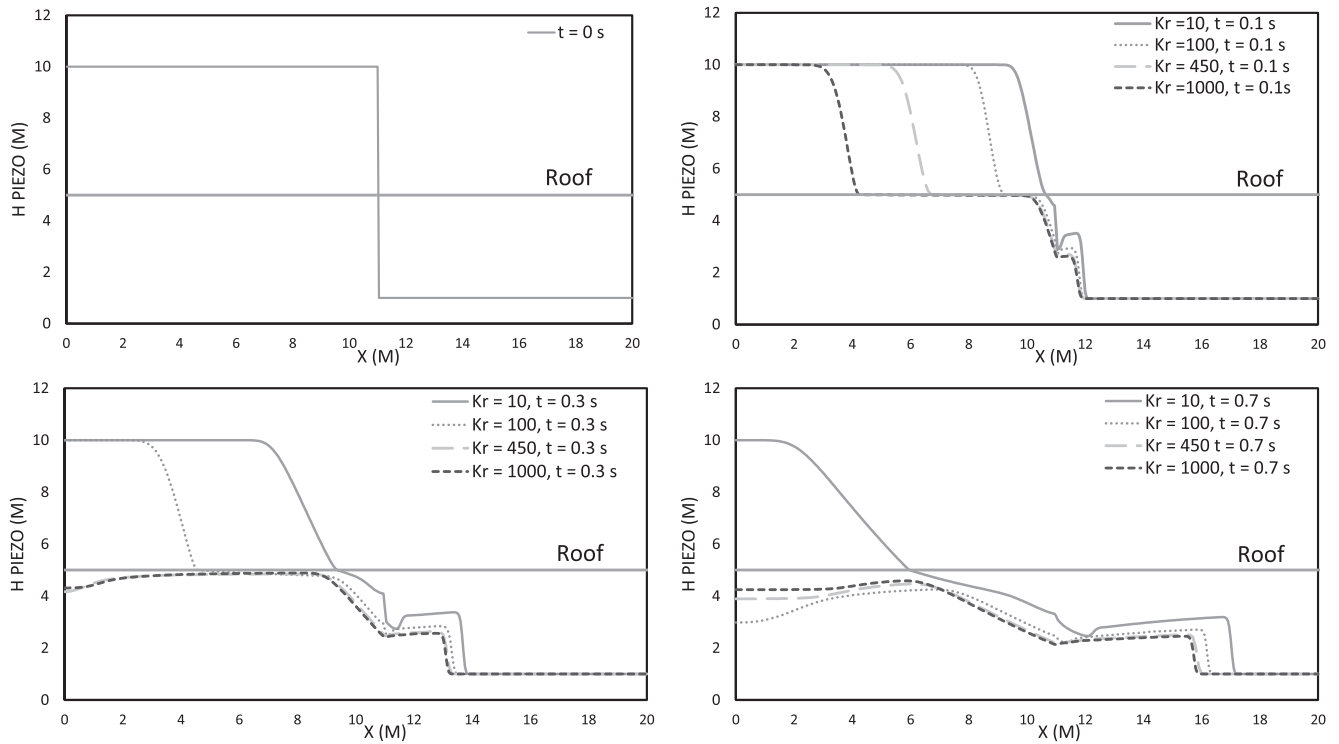
FIGURE 8 Test case T4. Comparison of the radial profiles of piezometric head at several time steps, computed with different values of the stiffness constant. Initial piezometric head (upper left), comparison at $t = 0.1$ s (upper right), $t = 0.3$ s (bottom left), and $t = 0.7$ s (bottom right)[18] [Colour figure can be viewed at wileyonlinelibrary.com]
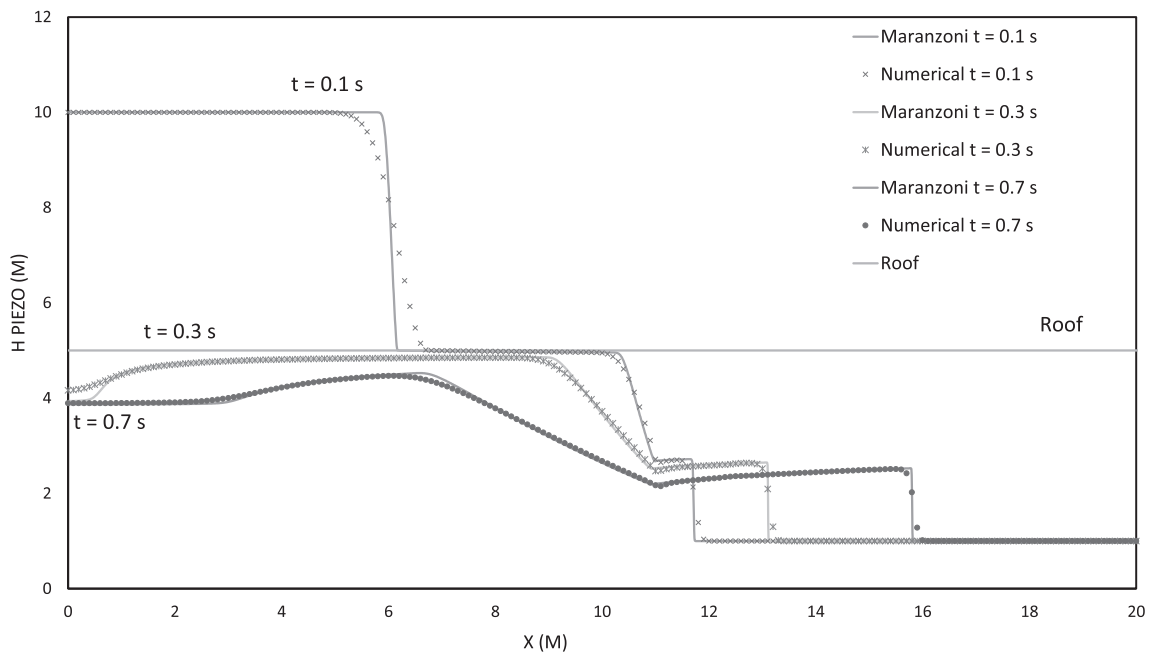
FIGURE 9 Test case T4. Radial profiles of piezometric head at several time steps. The numerical solution is compared with the reference solution presented in Reference 18 [Colour figure can be viewed at wileyonlinelibrary.com]
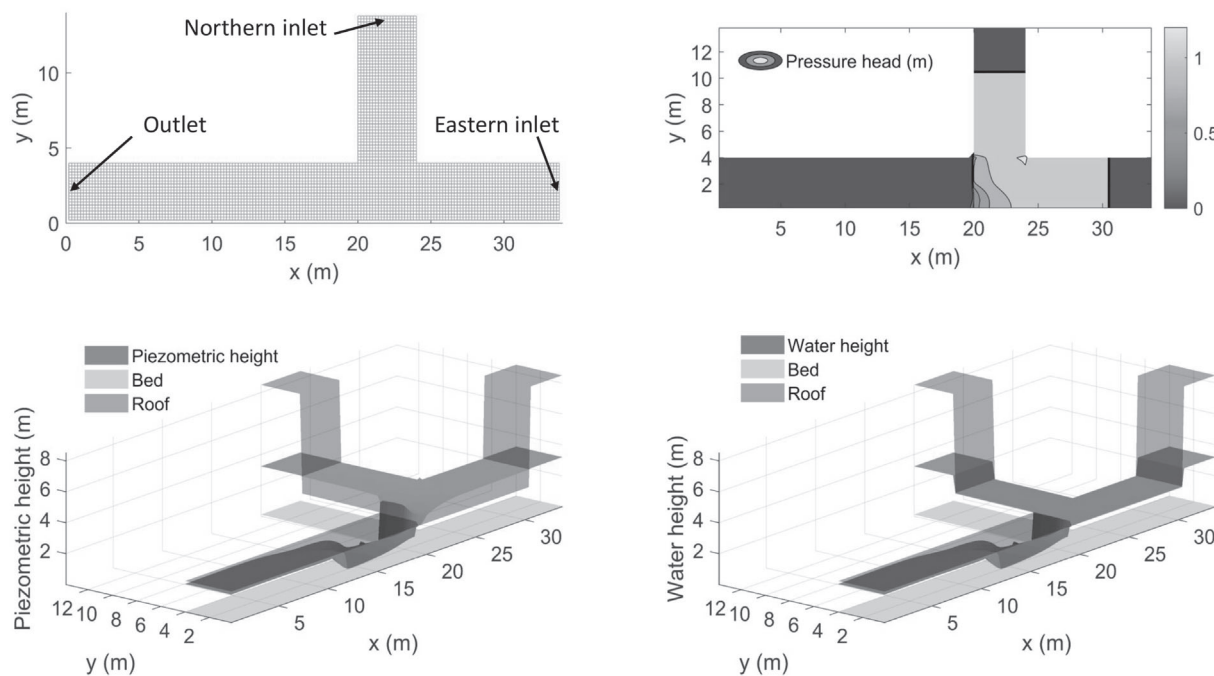
FIGURE 10 Test case T5. Channel junction at a 90° angle, with a total discharge of 20 m^3/s (10 m^3/s by each channel) and a water surface elevation at the outlet boundary of 1.80 m. Numerical mesh (upper-left); pressure head (m) computed as the difference between the piezometric head and the water surface elevation (upper right), piezometric head (lower left),and water surface elevation (lower right) [Colour figure can be viewed at wileyonlinelibrary.com]

As shown in Figure 11 (upper left), if the discharge is diminished to 15 m^3/s the hydraulic jump disappears and the pressure head at the inlet decreases by roughly 1 m (from 3.2 to 2.2 m). When the discharge is further diminished to 10 m^3/s, free surface conditions occur in the whole channel. The effect of the outlet boundary condition is also shown in Figure 11 (bottom left). Lowering the piezometric head at the outlet to the critical depth makes the hydraulic jump disappear and produces a decrease in the inlet piezometric head of roughly 0.7 m (from 3.2 to 2.5 m).

Overall, the proposed methodology is able to reproduce, without numerical instabilities, a physically correct behavior of the channel junction, including transitions from free surface to pressurized conditions and hydraulic jumps.

4.6 | Test case T6: Steady flow under a partially submerged beam bridge

This test case is based on one of the experimental cases presented in Reference 12, in which the flow through a beam bridge was studied experimentally. The case modeled here corresponds to the Deck 1 geometry from Reference 12, and its geometry is presented in Figure 12. This case was also studied numerically in Reference 55. The experiments were carried out in a smooth flat channel, 6 m long, with a 24 cm × 16 cm rectangular cross-section. The bridge deck width is 6 cm and is located 3 cm above the bed of the channel. Water levels were measured under steady conditions at two control points, located 1 m upstream, and 3 m downstream the center of the bridge.

The numerical domain consists of a rectangular channel of 5.8 m long and 24 cm wide. Two different inlet discharges and outlet conditions were tested, corresponding to cases in which the bridge is partially submerged (Table 2). Regarding the numerical discretization, the same conditions used in Reference 55 are used, namely, $\Delta x = \Delta y = 0.01$ m, a Courant number of 0.7, and a Manning's roughness coefficient of 0.011 s/m$^{1/3}$. The initial water level in the whole domain is set equal to the water level at the downstream boundary, and the simulation is run until the steady state is reached. A value of the roof stiffness constant equal to $K_r = 300$ m/s^2 was used.

The numerical backwater depth, computed as the absolute value of the difference between the measured values of the water depth at each gauge point, is shown in Table 2. The numerical results are slightly lower than those measured by Ratia et al.,[12] but similar to those computed by Maranzoni and Mignosa[55] using the Preissmann slot approximation. The
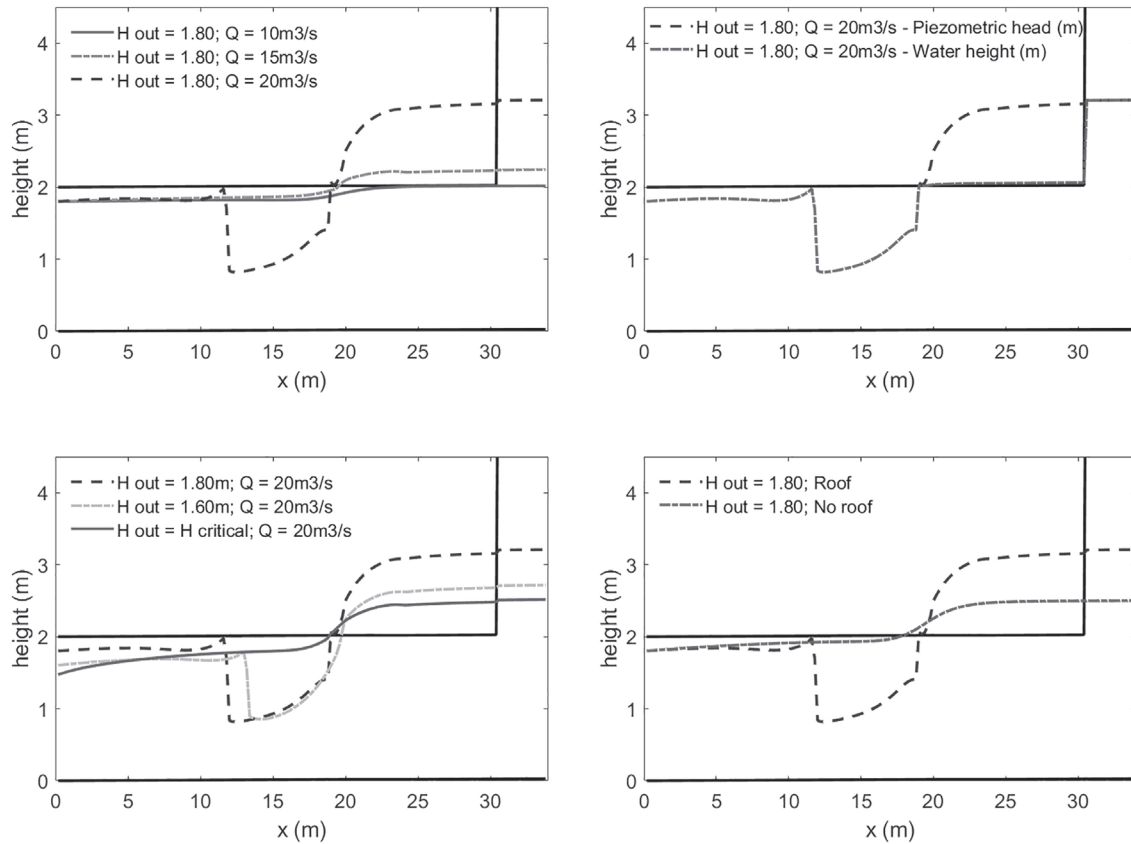
FIGURE 11 Test case T5. Longitudinal profiles along the main channel. Piezometric head for different discharges and a piezometric head at the outlet boundary of 1.80 m (upper left), piezometric head and water depth for a total discharge of 20 m^3/s and a piezometric head at the outlet boundary of 1.80 m (upper right), piezometric head for different outlet boundary conditions and a total discharge of 20 m^3/s (bottom left) and comparison between the results obtained with and without a roof for a total discharge of 20 m^3/s (bottom right) [Colour figure can be viewed at wileyonlinelibrary.com]

difference between observed and computed results might be ascribed to the local loss that occurs when the water hits the deck. The vertical acceleration and 3D local velocity pattern at that section cannot be reproduced by a 2D depth-averaged model and must be considered via a local loss coefficient. Local losses are usually evaluated as $\Delta H_l = \lambda \frac{|U|^2}{2g}$, where λ is a nondimensional losses coefficient between 0 and 1. In order to include a local loss at the control volume edge ij (Figure 2), we modified the total friction slope between the control volumes C_i and C_j located at the transition between free surface and pressurized flow as:

$$I_{x,ij} = \frac{n_c^2|\mathbf{U}|U_x}{h^{4/3}} + \frac{\lambda|\mathbf{q}|q_x}{2gh^2\Delta_{ij}} \quad I_{y,ij} = \frac{n_c^2|\mathbf{U}|U_y}{h^{4/3}} + \frac{\lambda|\mathbf{q}|q_y}{2gh^2\Delta_{ij}}, \tag{43}$$

where $(I_{x,ij}, I_{y,ij})$ are the two components of the total friction slope between the control volumes C_i and C_j, and Δ_{ij} is the distance between the geometric center of both control volumes. Notice that Equation (43) is applied only at the cell edges located at the transition between free surface and pressurized flow. If the previous local head loss is applied with $\lambda = 0.5$ at the cell faces that define the upwind side of the bridge deck, the computed backwater depth is much closer to the observed one, as shown in Table 2.

4.7 | Test case T7: Dam-break flow through an arch bridge

This test case is based on Experiment 10 described in Reference 12, where the dam-break flow under an arch bridge is studied experimentally. This case corresponds to the Arch 2 geometry from Reference 12, which is sketched in Figure 13.
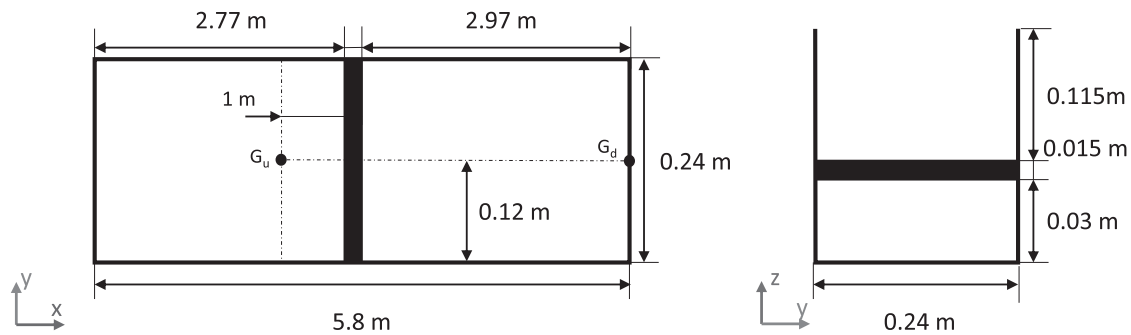
FIGURE 12 Test case T6. Plan view (left) and profile view (right) of the geometry used in the test case [Colour figure can be viewed at wileyonlinelibrary.com]

TABLE 2 Test case T6

	Experimental conditions		Backwater depth (cm)			
Case	Inlet discharge (L/s)	Outlet water depth (cm)	Observed	Maranzoni	Proposed methodology	Proposed methodology with $\lambda = 0.5$
a	2.5	2.7	1.0	0.86	0.87	1.00
b	3.056	3.1	1.1	0.90	0.85	1.09

Note: Boundary conditions and backwater depth observed and computed. Observed results from Reference 12. Maranzoni results refer to Reference 55.

The experiment was carried out in a closed, smooth, flat channel 6 m long, with a rectangular cross-section of 24 cm × 16 cm, connected to a rectangular reservoir with an horizontal section of 1.56 m × 0.84 m. The bottom of the reservoir is 12 cm below the bottom of the flume. The bridge deck is located at 1.646 m from the beginning of the channel and has a width of 6 cm. The arch of the bridge is 7.5 cm high.

The dam's gate is located between the reservoir and the main channel. Initially, the water depth in the reservoir is 18 cm, whereas in the main channel is 1.1 cm. The channel was closed downstream. Water levels were measured at two control points: G_u, located 1.510 m from the beginning of the channel (i.e., 0.136 m upstream of the bridge) and G_d, located 1.876 m from the beginning of the channel (i.e., 0.17 m downstream of the bridge). Both control points are located at the center line of the flume (Figure 13).

The physical domain is discretized using rectangular meshes with a spatial resolution of $\Delta x = \Delta y = 0.01$ m. The Courant number is set to 0.5 and the Manning's roughness coefficient to 0.011 s/m$^{1/3}$. A value of the roof stiffness constant equal to $K_r = 300$ m/s^2 was used.

After the dam break, a shock wave propagates through the flume until it reaches the bridge. This shock wave corresponds to the sharp increase in the water depth time series registered approximately 2 s after the dam break at G_u (Figure 14). The arrival time of this shock wave at G_u and its maximum depth are captured well by the model. Up to this time, the bridge has not influenced the flow and thus, the differences between numerical and experimental data are only due to the limitations of the shallow water assumptions. Once it reaches the bridge, the shock wave is reflected and returns upstream, generating a second increase in the water depth at G_u (registered approximately at $t = 12$ s in the numerical results). This second increase is not so sharp as the first one and is not so clearly reflected in the experimental data shown in Figure 14, probably due to the energy dissipation in the hydraulic jump front. The front shape of hydraulic jumps is not well captured by shallow water models due to the high local energy dissipation, air entrainment, and nonhydrostatic 3D effects, and this explains the differences between experimental and numerical data between $t = 10$ s and $t = 15$ s at G_u.

Regarding the downstream gauge station (G_d), the numerical model represents remarkably well the water depth evolution until 14 s after the dam break, except for the fact that some small numerical oscillations appear between $t = 9$ s and $t = 12$ s. These small spurious oscillations in the numerical time series also appear in References 12 and 55. At $t = 14$ s, a wave front appears in the experimental data, caused by the reflection of the flow in the downstream closed boundary of the flume. The numerical model gives a good prediction of the height of the shock front but with a time lag of approximately 1.5 s. This is because shallow water models do not provide the correct wave celerity when the hydrostatic pressure
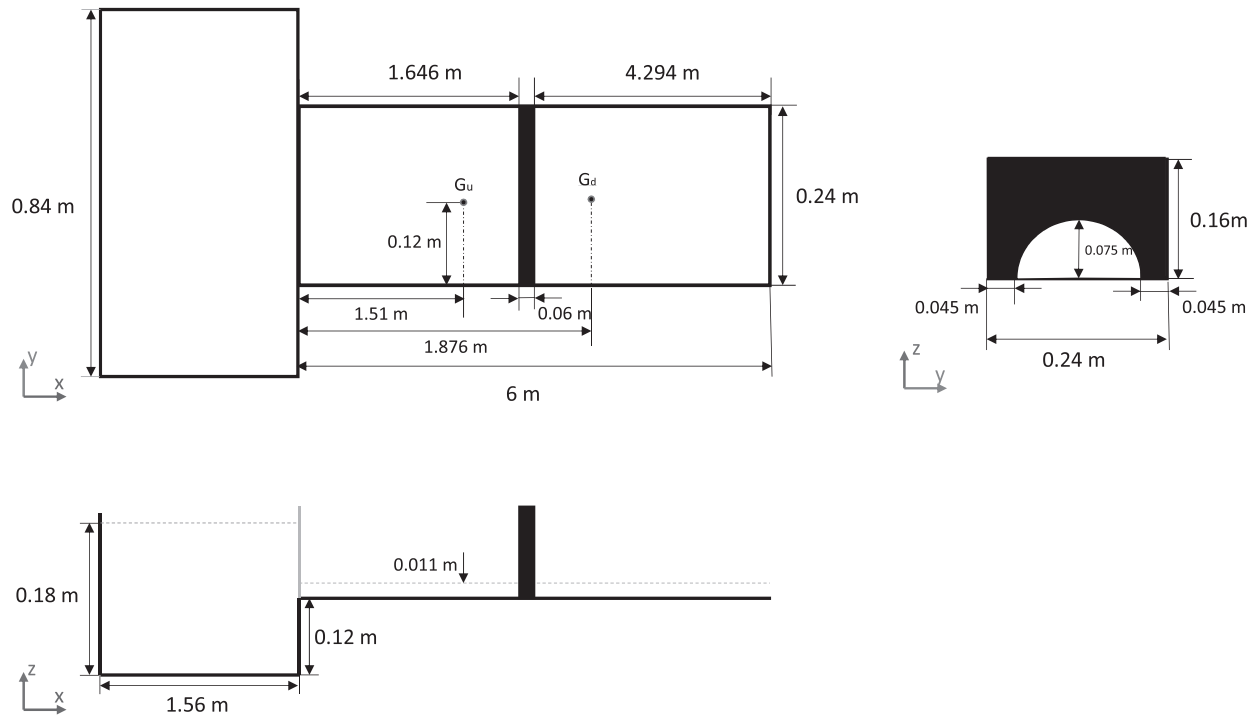
FIGURE 13 Test case T7. Plan view (upper left), profile view (upper right), and side view (bottom) of the geometry used in the test case [Colour figure can be viewed at wileyonlinelibrary.com]
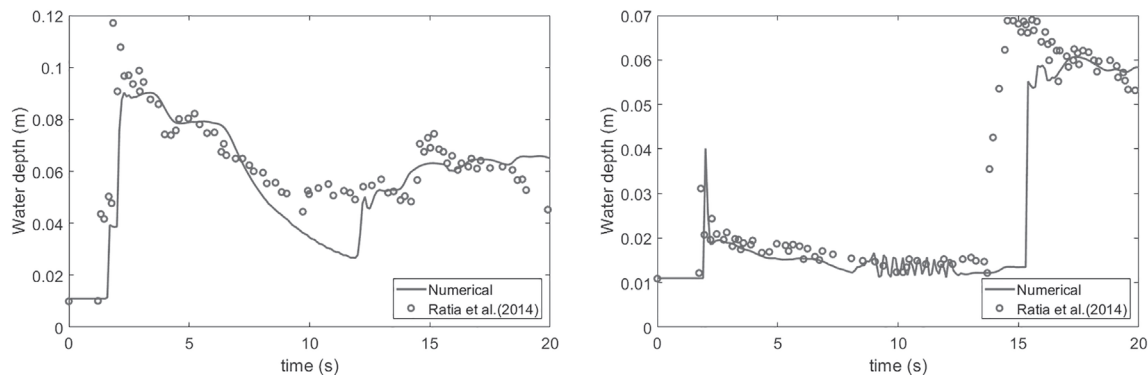
FIGURE 14 Test case T7. Water height time series at the upstream gauge station (left) and the downstream gauge station (right). The numerical solution is compared with the experimental data from experiment 10 presented in Reference 12 [Colour figure can be viewed at wileyonlinelibrary.com]

assumption is not fulfilled. A typical situation when this happens is when a surface wave or a supercritical flow impacts a closed wall generating high dynamic pressures, as reported in previous studies.[12,55,56]

5 | CONCLUSIONS

In this article we have presented a mathematical formulation to account for vertically confined flow conditions in 2D shallow water models, making it possible to compute 2D shallow water flows under mixed free-surface-pressurized conditions. The formulation proposed, which is an extension of the 1D TPA method, introduces a roof with a certain degree of elasticity, given by a user-defined stiffness constant, in order to compute a surface pressure which confines the vertical movement of the water column. The surface pressure exerted by the roof is included in the shallow water equations

by introducing a new source term and modifying the momentum flux. Hence, the proposed finite volume discretization for the modified shallow water equations changes the definition of the momentum flux in pressurized regions, according to the stiffness constant of the roof. This has direct implications in the wave celerity, and thus in the upwind discretization of the momentum flux. The proposed discretization is consistent and is able to reproduce the hydrostatic condition (C-property). The numerical stability restrictions are the same as those of an explicit finite volume solver for the standard shallow water equations (given by values of the CFL condition up to 1 in 1D problems, and up to 0.5 in 2D problems).

The method proposed here is an alternative to the Preissmann slot method in 2D simulations. Both methods introduce a certain distortion of the geometry (either as a roof elasticity or as a vertical slot) that depends on a numerical parameter, whose value can be theoretically fixed in order to reproduce the celerity of pressure waves in closed conduits. However, in practical applications the numerical parameter is fixed considering a compromise between numerical stability and accuracy. A difference between both methods is that in the 2D extension of the PSM the user needs to define two vertical slot widths, each of them parallel to one of the 2D Cartesian directions, while the 2D extension of the TPA needs just one numerical parameter, which makes it easier to implement in unstructured solvers. Apart from that, the main difference between both methods lies in the numerical schemes used to solve the modified shallow water equations.

The test cases presented here show that the proposed discretization is mass conservative and numerically stable, it preserves the hydrostatic solution (C-property), converges to analytical solutions when the stiffness constant of the roof is large enough, and reduces to a standard 2D-SWE solver under free surface conditions. Its ability to handle transient 2D mixed flows, including subcritical, supercritical, and transcritical conditions, has also been confirmed.

Overall, the proposed method can be considered as an improvement on standard 2D-SWE solvers that enables their application to transient mixed flows including free surface and vertically confined pressurized flows.

ACKNOWLEDGMENTS

ORCID

Luis Cea https://orcid.org/0000-0002-3920-0478
Alejandro López-Núñez https://orcid.org/0000-0002-4183-2917

REFERENCES

1. Bermudez M, Neal JC, Bates PD, et al. Quantifying local rainfall dynamics and uncertain boundary conditions into a nested regional-local flood modeling system. *Water Resour Res*. 2017;53(4):2770-2785.
2. Bodoque JM, Amérigo M, Díez-Herrero A, et al. Improvement of resilience of urban areas by integrating social perception in flash-flood risk management. *J Hydrol*. 2016;541:665-676.
3. Garrote J, Alvarenga FM, Díez-Herrero A. Quantification of flash flood economic risk using ultra-detailed stage-damage functions and 2-D hydraulic models. *J Hydrol*. 2016;541:611-625.
4. Ocio D, Stocker C, Eraso A, Martinez A, Galdeano JMS. Towards a reliable and cost-efficient flood risk management: the case of the Basque country (Spain). *Nat Hazards*. 2016;81(1):617-639.
5. Sanders BF, Schubert JE, Detwiler RL. ParBreZo: a parallel, unstructured grid, Godunov-type, shallow-water code for high-resolution flood inundation modeling at the regional scale. *Adv Water Resour*. 2010;33(12):1456-1467.
6. Sopelana J, Cea L, Ruano S. A continuous simulation approach for the estimation of extreme flood inundation in coastal river reaches affected by meso and macro tides. *Nat Hazards*. 2018;93(3):1337-1358.
7. Cea L, Puertas J, Vázquez-Cendón ME. Depth-averaged modelling of turbulent shallow water flow with wet-dry fronts. *Arch Comput Methods Eng*. 2007;14(3):303-341.
8. Chanson H. *Hydraulics of Open Channel Flow*. Elsevier; 2004. https://www.elsevier.com/books/hydraulics-of-open-channel-flow/chanson/978-0-7506-5978-9.
9. Sturm TW, Tuzson J. Open channel hydraulics; 2001:B107-B108.
10. Bladé E, Cea L, Corestein G, et al. Iber: herramienta de simulación numérica del flujo en ríos. *Revista Internacional de Métodos Numéricos para Cálculo y Diseño en Ingeniería*. 2014;30(1):1-10.
11. Costabile P., , Macchione F., Natale L., Petaccia G. Comparison of scenarios with and without bridges and analysis of backwater effect in 1-D and 2-D river flood modeling. *Comput Model Eng Sci* 2015;109(2):81-103.
12. Ratia H, Murillo J, García-Navarro P. Numerical modelling of bridges in 2D shallow water flow simulations. *Int J Numer Methods Fluids*. 2014;75(4):250-272.

13. Bousso S, Daynou M, Fuamba M. Numerical modeling of mixed flows in storm water systems: critical review of literature. *J Hydraul Eng*. 2013;139(4):385-396.

14. Cunge JA, Wegner M. Intégration numérique des équations d'écoulement de Saint-Venant's flow equations by means of an implicit scheme of finite differences. *La Houille Blanche*. 1964;1:33-39.

15. Kerger F, Archambeau P, Erpicum S, Dewals BJ, Pirotton M. A fast universal solver for 1D continuous and discontinuous steady flows in rivers and pipes. *Int J Numer Methods Fluids*. 2011;66(1):38-48.

16. Aureli F, Dazzi S, Maranzoni A, Mignosa P. Validation of single-and two-equation models for transient mixed flows: a laboratory test case. *J Hydraul Res*. 2015;53(4):440-451.

17. Malekpour A, Karney BW. Spurious numerical oscillations in the preissmann slot method: origin and suppression. *J Hydraul Eng*. 2015;142(3):04015060.

18. Maranzoni A, Dazzi S, Aureli F, Mignosa P. Extension and application of the Preissmann slot model to 2D transient mixed flows. *Adv Water Resour*. 2015;82:70-82.

19. Vasconcelos JG, Wright SJ, Roe PL. Improved simulation of flow regime transition in sewers: two-component pressure approach. *J Hydraul Eng*. 2006;132(6):553-562.

20. Sanders BF, Bradford SF. Network implementation of the two-component pressure approach for transient flow in storm sewers. *J Hydraul Eng*. 2011;137(2):158-172.

21. Casulli V, Stelling GS. A semi-implicit numerical model for urban drainage systems. *Int J Numer Methods Fluids*. 2013;73:600-614.

22. Wiggert DC. Transient flow in free-surface, pressurized systems. *J Hydraul Div*. 1972;98(1):11-27.

23. Fuamba M. Contribution on transient flow modelling in storm sewers. *J Hydraul Res*. 2002;40(6):685-693.

24. Politano M, Odgaard AJ, Kleecan W. Case study: numerical evaluation of hydraulic transients in a combined sewer overflow tunnel system. *J Hydraul Eng*. 2007;133(10):1103-1110.

25. Li J, McCorquodale A. Modelling mixed flow in storm sewers. *J Hydraul Eng*. 1999;125(11):1170-1180.

26. Li J, McCorquodale A. Modelling the transition from gravity to pressurized flows in sewers. *Urban Drainage Modeling*. Orlando, FL: ASCE; 2001:134-145.

27. Zhou F, Hicks F, Steffler P. Transient flow in a rapidly filling horizontal pipe containing trapped air. *J Hydraul Eng*. 2002;128(6):625-634.

28. Zhou F, Hicks F, Steffler P. Analysis of effects of air pockets on hydraulic failure of urban drainage infrastructure. *Can J Civ Eng*. 2004;31(1):86-94.

29. Bourdarias C, Gerbi S. A finite volume scheme for a model coupling free surface and pressurised flows in pipes. *J Comput Appl Math*. 2007;209(1):109-131.

30. Leon AS, Oberg N. *Illinois Transient Model: Two-Equation Model V.1.2, User's Manual*. EEUU: Boise State University College of Engineering; 2010.

31. Toro EF. *Shock-capturing Methods for Free-Surface Shallow Flows*. Chichester, England: Wiley; 2001.

32. Akbar M, Aliabadi S. Hybrid numerical methods to solve shallow water equations for hurricane induced storm surge modeling. *Environ Model Softw*. 2013;46:118-128.

33. Bertin X. Storm surges and coastal flooding: status and challenges. *La Houille Blanche*. 2016;2(2):64-70.

34. Bertin X, Olabarrieta M, McCall R. Hydrodynamics under storm. *Coastal Storms Processes Impact*. 2017;23:23-43.

35. Cea L. An unstructured finite volume model for unsteady turbulent shallow water flow with wet-dry fronts: numerical solver and experimental validation [Doctoral thesis]. Departamento de Métodos Matemáticos y de Representación Universidad de A Coruña; 2005.

36. Hinkelmann R. *Efficient Numerical Methods and Information-Processing Techniques for Modeling Hydro-and Environmental Systems*. Berlin, Germany: Springer Science & Business Media; 2006.

37. Pradhan S, Khatua KK. Composite roughness for rough compound channels. Riverflow; 2014.

38. Yen BC. Open channel flow resistance. *J Hydraul Eng*. 2002;128(1):20-39.

39. Versteeg HK, Malalasekera W. *An Introduction to Computational Fluid Dynamics. The Finite Volume Method*. Harlow, England: Pearson Education Ltd; 2007.

40. Chaudhry MH. *Applied Hydraulic Transients*. New York, NY: Springer; 1979.

41. LeVeque RJ. *Finite Volume Methods for Hyperbolic Problems*. Cambridge Texts in Applied Mathematics. Vol 31. Cambridge, MA: Cambridge University Press; 2002.

42. Toro EF. *Riemann Solvers and Numerical Methods for Fluid Dynamics: A Practical Introduction*. New York, NY: Springer-Verlag; 2009.

43. Courant R, Friedrichs K, Lewy H. On the partial difference equations of mathematical physics. *IBM J Res Dev*. 1967;11(2):215-234.

44. Bermúdez A, Dervieux A, Desideri JA, Vázquez-Cendón ME. Upwind schemes for the two-dimensional shallow water equations with variable depth using unstructured meshes. *Comput Methods Appl Mech Eng*. 1998;155:49-72.

45. Begnudelli L, Sanders BF, Bradford SF. An adaptive Godunov-based model for flood simulation. *J Hydraul Eng*. 2008;134(6):714-725.

46. Cea L, Vázquez-Cendón ME. Unstructured finite volume discretisation of two-dimensional depth-averaged shallow water equations with porosity. *Int J Numer Methods Fluids*. 2010;63(8):903-930.

47. Cea L, Vázquez-Cendón ME. Unstructured finite volume discretisation of bed friction and convective flux in solute transport models linked to the shallow water equations. *J Comput Phys*. 2012;231:3317-3339.

48. Cea L, Bladé E. A simple and efficient unstructured finite volume scheme for solving the shallow water equations in overland flow applications. *Water Resour Res*. 2015;51(7):5464-5486.

49. Guinot V, Soares-Frazao S. Flux and source term discretization in two-dimensional shallow water models with porosity on unstructured grids. *Int J Numer Methods Fluids*. 2006;50(3):309-345.

50. Sanders BF, Schubert JE, Gallegos HA. Integral formulation of shallow-water equations with anisotropic porosity for urban flood modeling. *J Hydrol*. 2008;362:19-38.

51. Roe PL. Discrete models for the numerical analysis of time-dependent multidimensional gas dynamics. *J Comput Phys*. 1986;63:458-476.

52. Cea L, Garrido M, Puertas J. Experimental validation of two-dimensional depth-averaged models for forecasting rainfall-runoff from precipitation data in urban areas. *J Hydrol*. 2010;382:88-102.

53. Marche F, Bonneton P, Fabrie P, Seguin N. Evaluation of well-balanced bore-capturing schemes for 2D wetting and drying processes. *Int J Numer Methods Fluids*. 2007;53(5):867-894.

54. Bermúdez A, Vázquez-Cendón ME. Upwind Methods for Hyperbolic Conservation Laws with Source Terms. *Comput Fluids*. 1994;23(8):1049-1071.

55. Maranzoni A, Mignosa P. Numerical treatment of a discontinuous top surface in 2D shallow water mixed flow modeling. *Int J Numer Methods Fluids*. 2018;86(4):290-311.

56. Cea L, Ferreiro A, Vázquez-Cendón ME, Puertas J. Experimental and numerical analysis of solitary waves generated by bed and boundary movements. *Int J Numer Methods Fluids*. 2004;46(8):793-813.